UNIVERSITY OF CALIFORNIA, SAN DIEGO

Piezoelectric Nanoparticle-Polymer Composite Materials

A Thesis submitted in partial satisfaction of the requirements
for the degree Master of Science

in

Nanoengineering

by

William Ray McCall

Committee in charge:

Professor Donald Sirbuly, Chair
Professor Darren Lipomi
Professor Andrea Tao

2014

The Thesis of William Ray McCall is approved, and it is acceptable in quality and form for publication on microfilm and electronically:

_____

_____

_____

Chair

University of California, San Diego

2014

EPIGRAPH

"I want to stand as close
to the edge as I
can without going over.
Out on the edge you see all
the kinds of things you can't
see from the center."

Kurt Vonnegut

TABLE OF CONTENTS

Signature Page iii
Epigraph iv
Table of Contents v
List of Figures & Tables vi
Acknowledgements viii
Abstract of the Thesis ix
Introduction 11
References 12
1 Piezoelectric Nanoparticle-Polymer Composite Foams 14
1.1 Introduction 14
1.2 Materials Synthesis and PNPF Mechanical Properties 15
1.2.1 Barium Titanate Nanoparticle Synthesis 16
1.2.2 Powder X-ray Diffraction of BTO Nanoparticles 17
1.2.3 Piezoelectric Nanoparticle-Polymer Foam Synthesis 19
1.3 Electro-mechanical Characterization of PNPFs 24
1.3.1 Electronic Characterization 24
1.3.2 Decoupling the Triboelectric Effect 28
1.3.3 PNPF Charge Dynamics 30
1.3.4 PNPF Power Generation 32
1.4 Conclusions 35
1.5 References 36
2 3D Optical Printing of Piezoelectric Nanoparticle-Polymer Composite Materials 39
2.1 Introduction 39
2.2 Materials Synthesis and Photofabrication Process 42
2.2.1 Preparation of PEGDA and BTO Nanoparticle Composites 42
2.2.2 FTIR Spectra of TMSPM-grafted BTO Nanoparticles 44
2.2.3 Optical Printing and Film Preparation 45
2.3 Photofabrication Results and Characterization 46
2.3.1 2D Structures 46
2.3.2 3D Structures 47
2.3.3 Electrical Response 50
2.4 Conclusions 55
2.5 References 57

LIST OF FIGURES & TABLES

Figure 1. XRD pattern of the as-made BTO nanoparticles (red) and a reference $BaTiO_3$ pattern (black). The XRD spectra indicate that the nanoparticles have a strong tetragonal phase given their c/a ratio of 1.007. 18

Figure 2. (a,b) Schematics of the capillary-action (a) and roll-out (b) methods of creating PNPFs. (c) Digital images of PNPFs created with the capillary-action method (left) and the roll-out method (middle). (d) Scanning electron micrographs of a 50% (left) and 73% (right) PNPF. 21

Table 1. A table showing the various sugar/composite ratios and the respective porosities determined using the methanol saturation method. 21

Figure 3. Model of sugar/composite ratio with respect to the porosity. 22

Figure 4. Compressive stress vs strain curves for (a) pure PDMS foam and (b) PNPF. .. 23

Figure 5. Cycling data of a 73% porous PNPF cube after 1200 cycles showing minimal loss to its modulus. The sample was compressed with a 10 N load at 20% strain. .. 24

Figure 6. (a) Schematic of the poling process. (b) Cycling data for a 73% foam showing the piezoelectric output and applied force vs time as a rod is dropped (c) Effective piezoelectric coefficient (d_{33}) of the PNPFs as a function of porosity. The neat film (0% porosity) is also shown for comparison. 25

Figure 7. (a) Schematic of the FlexiForce® sensor (Tekscan) circuit (b) Calibration curve of the force sensor. (c) Schematic of the charge amplifier used in the home-build piezo-testing apparatus. 27

Figure 8. Plots showing the electrical response of various electrode/sample interfaces to understand the effects of contact, or static, charge generation (i.e., triboelectric effect). By using the composite resins on the electrodes, instead of pure PDMS, it was found that the static charges could be eliminated. 29

Figure 9. (a) Single charge/discharge traces (7 ms each) for a 0%, 50%, 62%, and 73% porous film. The applied force is also plotted in real–time. (b) Time difference between peak voltage and force as a function of porosity. Also plotted is the compressive strain rate of the foam as a function of porosity under a ~ 10 N load. 31

Figure 10. (a) Power output as a function of external load for different porosity films and a neat film. A ~ 10 N load is being applied to the samples. (b) Plot showing the charging up of a 100 nF capacitor. The voltage and 118 Hz impulse force are plotted as a function of time. 34

Figure 11. (a) Schematic of the DPP setup that projects dynamic digital masks on the photoliable piezoelectric nanoparticle-polymer composite solution. (b) Scanning electron micrograph of BTO nanoparticles grown via a hydrothermal process. (c) Cartoon showing the piezoelectric polymer composite materials. 43

Figure 12. The chemical structure of TMSPM (top left) and FTIR spectra of pure TMSPM (blue), as-made BTO nanoparticles (black), and TMSPM-grafted BTO nanoparticles (red). 44

Figure 13. Collage of piezoelectric microstructures printed using DPP including a (a) dot array, (b-c) square arrays with different sized void spaces, and (d) a honeycomb array. All structures were fabricated in < 2 seconds using a PEGDA solution loaded with 1 % of the TMSPM-modified BTO nanoparticles. 47

Figure 14. Various 3D structures fabricated by DOPsL including (a) a mushroom-like array, (b) a cross array, and (c) a tapered cantilever array (dark region – cantilever; light region - support). (d) A microtubule structure formed by releasing a honeycomb array from the substrate. 49

Figure 15. UV-Vis spectra of pure PEDGA (green) and PEGDA/BTO composite solutions; 1 % (black), 5 % (red), and 10% (blue). The transmittance is directly related to the BTO loading fraction and shows higher transmission at longer wavelength. 50

Figure 16. (a) Voltage response of various unpoled and poled composite materials (neat films) cycled with a 1.44 N load applied perpendicular to the surface of the film. (b) Plot showing the effective piezoelectric modulus (d_{33}) of a grafted PEGDA/BTO composite material as a function of BTO mass loading. 52

Figure 17. Voltage response of a 5% BTO loaded PEGDA honeycomb array (similar structure to Figure 2d) fabricated by DPP. 53

ACKNOWLEDGEMENTS

I would like to acknowledge Professor Donald Sirbuly for his support during my tenure in his lab and as the chair of my committee. His guidance has proved to be invaluable.

I would like to thank my parents for lending me their full support throughout this entire journey. None of this would have been possible if it weren't for both of you.

Chapter 1, in full, is a modified reprint of the material as it appears in ACS Applied Materials & Interfaces 2014. W.R. McCall was the primary investigator and author of this paper.

Chapter 2, in full, is a modified reprint of the material as it appears in ACS Nano 2014. Kim, K., Zhu, W., Qu, X., Aaronson, C., Chen, S., Sirbuly, D. J. are the co-authors of this material.

ABSTRACT OF THE THESIS

Piezoelectric Nanoparticle-Polymer Composite Materials

by

William Ray McCall

Master of Science in Nanoengineering

University of California, San Diego, 2014

Professor Donald Sirbuly

Herein we demonstrate that efficient piezoelectric nanoparticle-polymer composite materials can be synthesized and fabricated into complex microstructures using sugar-templating methods or optical printing techniques. Stretchable foams with excellent tunable piezoelectric properties are created by incorporating sugar grains directly into polydimethylsiloxane (PDMS) mixtures containing barium titanate ($BaTiO_3$ – BTO) nanoparticles and carbon nanotubes (CNTs), followed by removal of the sugar

after polymer curing. Porosities and elasticity are tuned by simply adjusting the sugar/polymer mass ratio and the electrical performance of the foams showed a direct relationship between porosity and the piezoelectric outputs. User defined 2D and 3D optically printed piezoelectric microstructures are also fabricated by incorporating BTO nanoparticles into photoliable polymer solutions such as polyethylene glycol diacrylate (PEGDA) and exposing to digital optical masks that can be dynamically altered. Mechanical-to-electrical conversion efficiency of the optically printed composite is enhanced by chemically altering the surface of the BTO nanoparticles with acrylate groups which form direct covalent linkages with the polymer matrix under light exposure. Both of these novel materials should find exciting uses in a variety of applications including energy scavenging platforms, nano- and microelectromechanical systems (NEMS/MEMS), sensors, and acoustic actuators.

Introduction

Mechanically flexible piezoelectric materials are highly sought after when building advanced sensors, actuators, and energy scavenger devices. The most common piezoelectric materials used in applications are focused on electroceramic thin films made from lead zirconate titanate [$Pb(Zr_xTi_{x-1})O_3$ – also known as PZT) or barium titanate ($BaTiO_3$ – BTO). Although these materials can have large piezoelectric moduli (d_{33}; which is the induced polarization along the poled axis over the applied stress along the same axis), with PZT reaching values > 300 pC/N[1] and BTO exceeding 200 pC/N depending on ceramic type and processing conditions,[2-3] as thin films they are extremely brittle and difficult to shape into highly mechanically compliant structures. Improving mechanical flexibility of piezoelectrics, and creating higher order structures, is critical for driving new applications such as biological energy harvesting, compact acoustic transducers, and *in vivo* biodiagnostics. In recent years there has been significant progress on making brittle electroceramics such as PZT more flexible by reducing the size of the piezoelectrics and fabricating high density arrays.[4-5] For example, McAlpine *et al.* demonstrated that PZT nanoribbons could be patterned on elastomers over large areas while maintaining effective piezoelectric coefficients of > 100 pC/N for efficient energy scavenging devices.[4] Similar materials could also be suspended across trenches to probe cellular deformation with nanonewton force resolution.[6] Beyond perovskite-based ceramics, piezoelectric semiconductor oxides such as ZnO nanowire arrays have also been heavily researched for various applications including energy harvesting,[7-8] electronics,[9] and sensing.[10] However, systems that rely on one-dimensional

nanostructures to enhance mechanical flexibility limit the number of stress directions which can produce piezoelectric fields. If structures can be fabricated with higher piezoelectric symmetry (i.e., macroscopic structure is similar in all direction), and more mechanically compliant materials, it is anticipated that the piezoelectric sensitivity will increase which will lead to host of exciting applications.

References

1 Jaffe, B.; Cook, W. R.; Jaffe, H., *Piezoelectric Ceramics*. Academic Press: London, 1971.

2 Takahashi, H.; Numamoto, Y.; Tani, J.; Matsuta, K.; Qiu, J. H.; Tsurekawa, S. Lead-Free Barium Titanate Ceramics with Large Piezoelectric Constant Fabricated by Microwave Sintering. *Jpn. J. Appl. Phys., Part 2* **2006,** *45*, L30-L32.

3 Wada, S.; Yako, K.; Kakemoto, H.; Tsurumi, T.; Kiguchi, T. Enhanced Piezoelectric Properties of Barium Titanate Single Crystals with Different Engineered-Domain Sizes. *J. Appl. Phys.* **2005,** *98*, 014109.

4 Qi, Y.; Jafferis, N. T.; Lyons, K., Jr.; Lee, C. M.; Ahmad, H.; McAlpine, M. C. Piezoelectric Ribbons Printed onto Rubber for Flexible Energy Conversion. *Nano Lett.* **2010,** *10*, 524-528.

5 Xu, S.; Hansen, B. J.; Wang, Z. L. Piezoelectric-Nanowire-Enabled Power Source for Driving Wireless Microelectronics. *Nat. Commun.* **2010,** *1*, 1-5.

6 Nguyen, T. D.; Deshmukh, N.; Nagarah, J. M.; Kramer, T.; Purohit, P. K.; Berry, M. J.; McAlpine, M. C. Piezoelectric Nanoribbons for Monitoring Cellular Deformations. *Nat. Nanotechnol.* **2012,** *7*, 587-593.

7 Xu, S.; Qin, Y.; Xu, C.; Wei, Y. G.; Yang, R. S.; Wang, Z. L. Self-Powered Nanowire Devices. *Nat. Nanotechnol.* **2010,** *5*, 366-373.

8 Wang, X. Y.; Kim, K.; Wang, Y. M.; Stadermann, M.; Noy, A.; Hamza, A. V.; Yang, J. H.; Sirbuly, D. J. Matrix-Assisted Energy Conversion in Nanostructured Piezoelectric Arrays. *Nano Lett.* **2010,** *10*, 4901-4907.

9 Wang, Z. L. Progress in Piezotronics and Piezo-Phototronics. *Adv. Mater.* **2012,** *24*, 4632-4646.

10 Wang, Z. L. Self-Powered Nanosensors and Nanosystems. *Adv. Mater.* **2012,** *24*, 280-285.

1 Piezoelectric Nanoparticle-Polymer Composite Foams

*ACS Applied Materials and Interfaces 2014

1.1 Introduction

Foams, which are basically intact materials with large void fractions (e.g., 50 – 80% air), offer a unique means of creating materials with similar structuring in all dimensions. Most foams can be considered a solid (or liquid) material with a random network of air channels. For piezoelectrics this typically involves generating ceramic materials through fused-deposition[1] or robocasting[2] techniques which can be refined to create well-controlled porous structures either by layer-by-layer or polymeric templating.[3] Interestingly, it was found that the PZT foams have higher piezo-sensitivity, lower acoustic impedance, and high mechanical flexibility compared to their thin film counterparts, which have inspired a host of applications including wide-band hydrophones, actuators, and high-temperature filters.[4-6] Although porosity enhances many of the electrical and mechanical properties of electroceramics, they are still very brittle and cannot be strained beyond a few percent. Therefore it is of interest to investigate alternative materials that can offer high piezoelectric coefficients while maintaining elasticity and isotropic mechanical integrity, as well as cost-effective synthetic strategies.

Of the many piezoelectric material types, polymers have not been as heavily researched compared to the electroceramics but can offer many advantages over the ceramics including solution-based processability, biocompatibility, and high elasticity. The most well-known piezoelectric polymer is polyvinylidene fluoride (PVDF)[7] which

has a piezoelectric coefficient (d_{33} ~ -20 to -34 pC/N) that is about an order of magnitude smaller than PZT. Because of its electrical and mechanical properties, PVDF is being pursued for a wide range of applications including non-volatile low voltage memory,[8] hydrophones and acoustic transmitters,[9-10] and implantable medical devices.[11] To improve flexibility and integration capability, PVDF can be electrospun into fibers which has led to various energy harvesting devices.[12-14] PVDF foams with similar piezoelectric coefficients to the thin films and fibers have also been investigated; leading to efficient energy harvesters for sound.[15] Beyond the pure polymers such as PVDF, there have been advances with other polymer systems such as piezoelectric composites that combine electroceramic nanoparticles with a polymer matrix. For example, Lee *et al.* demonstrated that BTO nanoparticles could be mixed with an elastomer such as polydimethylsiloxane (PDMS) and carbon nanotubes (CNTs) to create highly flexible and efficient piezoelectric materials for energy harvesting.[16] The role of the CNTs in these composites was to enhance the stress transfer from the polymer to the BTO nanoparticles. Our group has further advanced these types of composite materials by demonstrating that they can be optically printed into user-defined 2D and 3D microstructures with strong piezoelectric properties.[17]

1.2 Materials Synthesis and PNPF Mechanical Properties

In this work we investigate strategies to create highly elastic piezoelectric polymers that maintain 3D structural isotropy and strong piezoelectric behavior. Our approach combines simple foam processing with piezoelectric polymer composites so we can control the mechanical and electrical properties of the materials. Over the past few years researchers have been investigating porous elastomers such as PDMS for

membrane separation and oil absorbent applications.[18-20] Of the various fabrication techniques for producing PDMS foams, the sugar-template method described by Choi *et al.* provides a simple and cost effective procedure to making highly porous polymer materials.[19] A variant of ancient casting methods, here commercially available sugar is added to the PDMS mixture which can then be easily removed by soaking in water, leaving a 3D isotropic network of air channels in the polymer. The porous materials created with this method are extremely soft with an elastic modulus of ~ 20 kPa which is well over an order of magnitude smaller than bulk PDMS (~ 750 kPa). Here we leverage similar sugar-templating strategies to fabricate piezoelectric nanoparticle-polymer composite foams (PNPFs) and systematically study their porosity and mechanical properties and correlate these with the piezoelectric performance of the materials.

1.2.1 Barium Titanate Nanoparticle Synthesis

The BTO nanoparticles synthesis was adapted from a previously reported solvo-thermal method.[21] In a 50 mL Teflon liner 7.102 g (37.5 mmol) of barium hydroxide monohydrate ($Ba(OH)_2$-H_2O, 98%, Aldrich) was added to 12.5 mL of DI water and stirred at 80 ^oC until a slurry was formed. The liner was transferred to a glovebox (21 ^oC, ~ 8% humidity) and a solution containing 8.509 g (25 mmol) of titanium-butoxide ($Ti[OCH_2CH_2CH_2CH_3]_4$, Aldrich) in 10 mL of high purity ethanol and 3.5 ml of ammonia hydroxide (28-30% NH_3 in water) was added. Additionally 2.5 mL of diethanolamine ($HN(CH_2CH_2OH)_2$, Aldrich) was mixed into the final solution to ensure highly tetragonal and monodisperse nanoparticles while also suppressing growth. The Teflon liner was sealed in a stainless steel pressure vessel inside the glove box and placed in an oven for 16 hours at 200 ^oC. After the reaction, the contents of the Teflon liner were

washed and vacuum filtered 3 times with DI water and 3 times with ethanol. The nanopowder was then vacuum dried for 24 hours before use.

1.2.2 Powder X-ray Diffraction of BTO Nanoparticles

In order to confirm a ferroelectric crystal structure of the BTO NPs, powder X-ray diffraction (XRD) spectra were recorded using a Bruker D8 X-ray diffractometer. It is important that the nanoparticles exhibit a tetragonal crystal structure because this allows them to be electrically poled more efficiently. Compared to the paraelectric, cubic phase, randomly oriented dipoles in the tetragonal phase are more easily aligned in an electric field. In other words, it requires more energy to create a dipole in the cubic crystal than it does to realign an already existing dipole in the tetragonal crystal. Figure 1 shows X-ray diffraction patterns of the as-made BTO nanoparticles and a reference $BaTiO_3$ pattern.[22] In order to detect tetragonality in the system we examine the diffraction peak in the (002) plane. The reference sample (black) shows a single peak associated with the c parameter of a perovskite crystal. In the as-made sample (red) a small shoulder appears, which can be attributed to peak splitting. This new peak is shifted to a lower 2θ value indicating an increase in spacing of the (002) planes in the crystals. This elongation of the crystal structure along the c axis changes the c/a ratio from 1 to 1.007 and is proof of tetragonality.

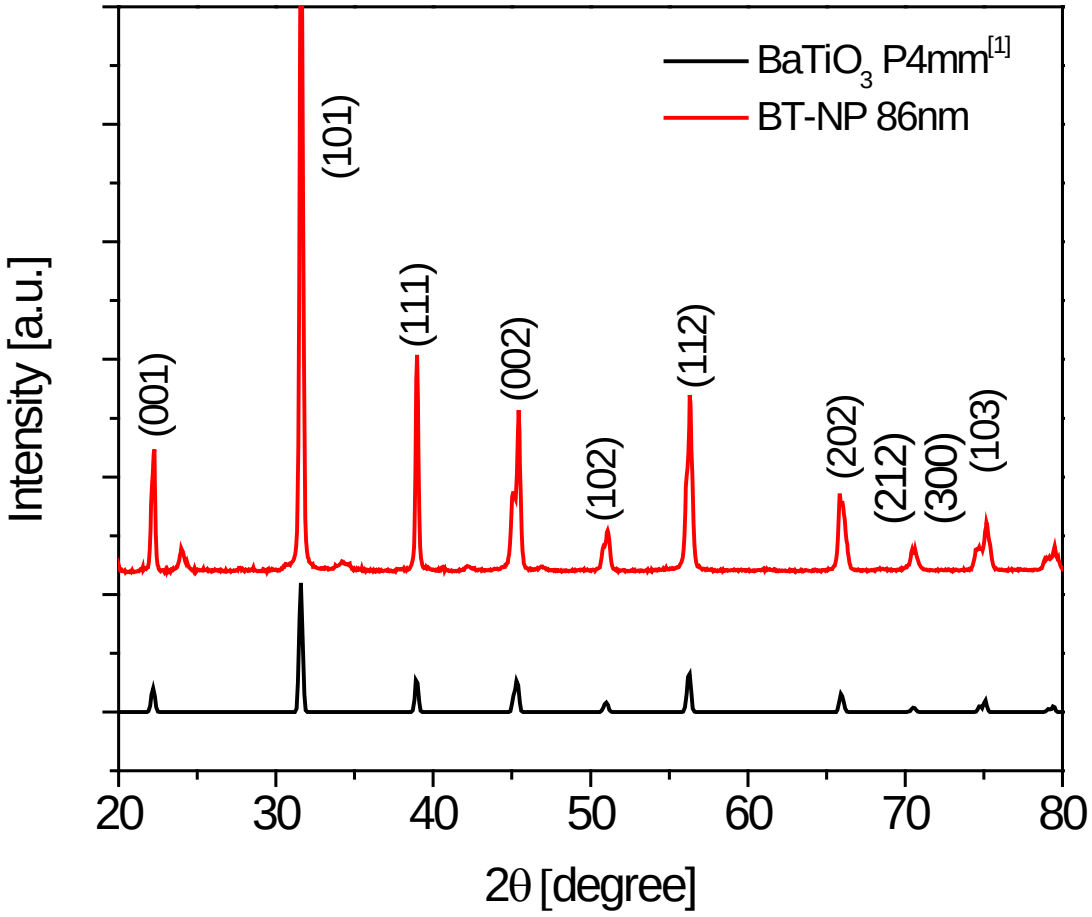

Figure 1. XRD pattern of the as-made BTO nanoparticles (red) and a reference $BaTiO_3$ pattern (black). The XRD spectra indicate that the nanoparticles have a strong tetragonal phase given their c/a ratio of 1.007.

1.2.3 Piezoelectric Nanoparticle-Polymer Foam Synthesis

We investigated two variants of the foam processes. Composite mixtures were made by combining 10% wt. BTO nanoparticles and 1% wt. multi-walled carbon nanotubes with polydimethylsiloxane (PDMS; Sylgard 184, Dow) similar to previous reports.[16] To ensure a well-mixed solution, the composites were sonicated for a minimum of 5 hours. The resulting composite resin was dark gray with a slightly higher viscosity than pure PDMS. To create the foams, either a capillary-action or roll-out method was used. In the capillary-action method, and similar to previously reported techniques,[19] a standard sugar cube was dropped into the PDMS composite and placed in a vacuum desiccator for ~ 2 hours. After infiltration the cube was placed in a 100 °C furnace for 10 minutes to cure the PDMS, followed by a 1 hour soak in boiling water to remove the sugar (Figure 2a). This method works well for creating large volume foam structures, but the limitations of the technique include not being able to fine tune the porosity and it is challenging to generate high electric fields across the material to align the dipoles in the BTO nanoparticles without significantly compressing the material or using extremely high voltages (> 10 kV). To better control the porosity and allow thinner films to be fabricated with higher throughput, free sugar can be added directly to the uncured polymer composite and rolled out once the proper viscosity is reached (Figure 2b). For the roll-out method, ultrafine baker's sugar (~ 150 μm diameter sugar particles) was mixed into the polymer resin until a soft dough formed. The dough was placed on a sheet of Kapton film and rolled out to a desired thickness of 300 — 400 μm using a round Teflon beaker. Ratios of 1.8 to 4.4 g sugar per gram of resin were used to achieve the desired porosities. The sheets were placed in the oven at 100 ^{o}C for 10 minutes to ensure

complete curing. In order to create the foam structure the fully cured sheets were placed in boiling water to dissolve the sugar, washed in ethanol and dried in an oven at 100 ^{o}C. Table 1 and Figure 3 show a table and plot, respectively, of sample porosities resulting from various sugar/polymer ratios. The porosities were calculated using a methanol saturation method[23]:

$$\phi = [\rho_{sat} - \rho_{dry}]/\rho_{methanol}$$

where ρ_{dry}, ρ_{sat}, and $\rho_{methanol}$ are the densities of the dry foam, methanol-saturated foam, and methanol, respectively. The value used for $\rho_{methanol}$ is 0.7918 g/cm^3. Lower porosities were difficult to achieve since the materials would contain trapped pockets of sugar which could not be removed. The pore size is governed by the sugar grain size and can be kept constant by infusing the same sugar type regardless of the sugar/polymer ratio (Figure 2d). To limit pore size distribution we only used fine baker's sugar. Other sugar types (e.g., powdered, granulated) were experimented with, but ultimately led to inferior or unusable materials. As expected, the foam stiffness is directly related to porosity showing elastic moduli ranging from 248 kPa for the 50% porous composites to 32 kPa for the foams with 73% porosity (Figure 4). The composite foams show slightly higher stiffness values compared to pure PDMS foams due to the addition of BTO nanoparticles and CNTs. The foams also show excellent cyclability without any significant change in the elastic properties after repeated strain curves (1,200 cycles)(Figure 5). This is important for piezoelectric applications that require repeated compression or tension to generate charge and power.

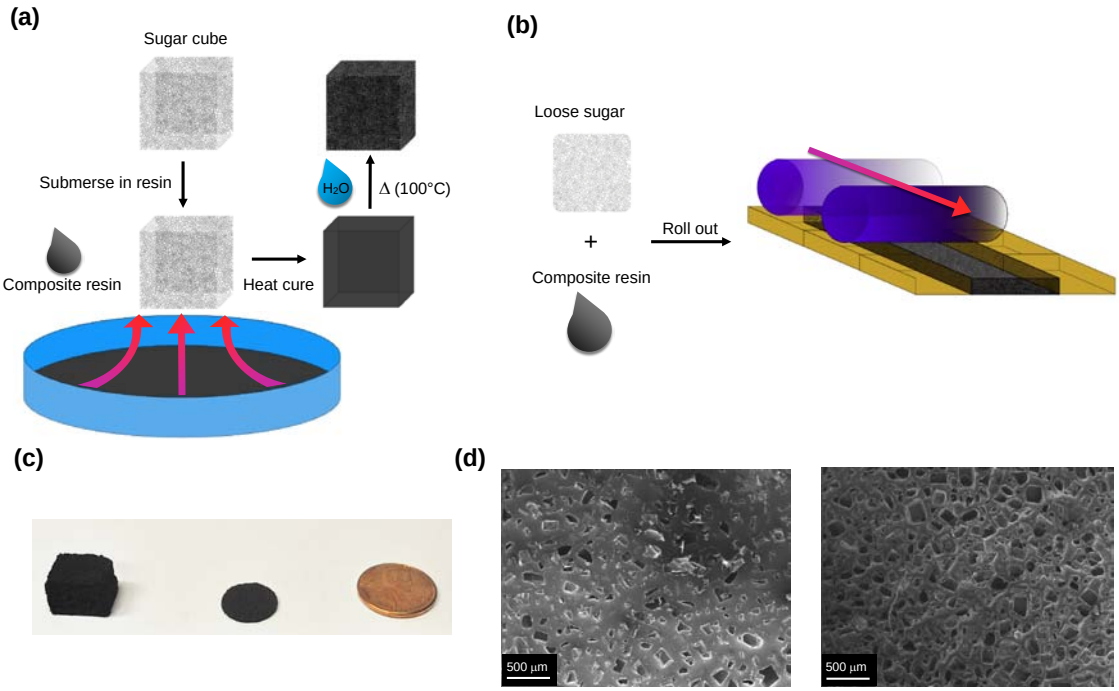

Figure 2. (a,b) Schematics of the capillary-action (a) and roll-out (b) methods of creating PNPFs. (c) Digital images of PNPFs created with the capillary-action method (left) and the roll-out method (middle). (d) Scanning electron micrographs of a 50% (left) and 73% (right) PNPF fabricated from the roll-out method using the same sugar grain size.

Table 1. A table showing the various sugar/composite ratios and the respective porosities determined using the methanol saturation method.

Sample	Sugar:Composite Resin (g:g)	ρ_{dry} (g/cm^3)	ρ_{sat} (g/cm^3)	ϕ (%)
1	1.8	0.489	0.8753	48.8
2	2.4	0.2933	0.7846	62.04
3	2.8	0.2462	0.7475	63.32
4	3.2	0.2638	0.7917	66.67
5	3.6	0.2085	0.8133	71.88
6	4	0.2154	0.7471	73.04
7	4.4	0.1966	0.78	73.68

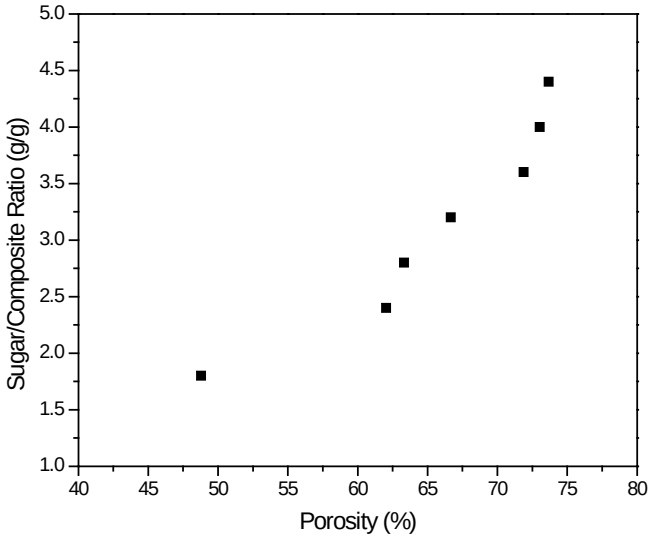

Figure 3. Model of sugar/composite ratio with respect to the porosity.

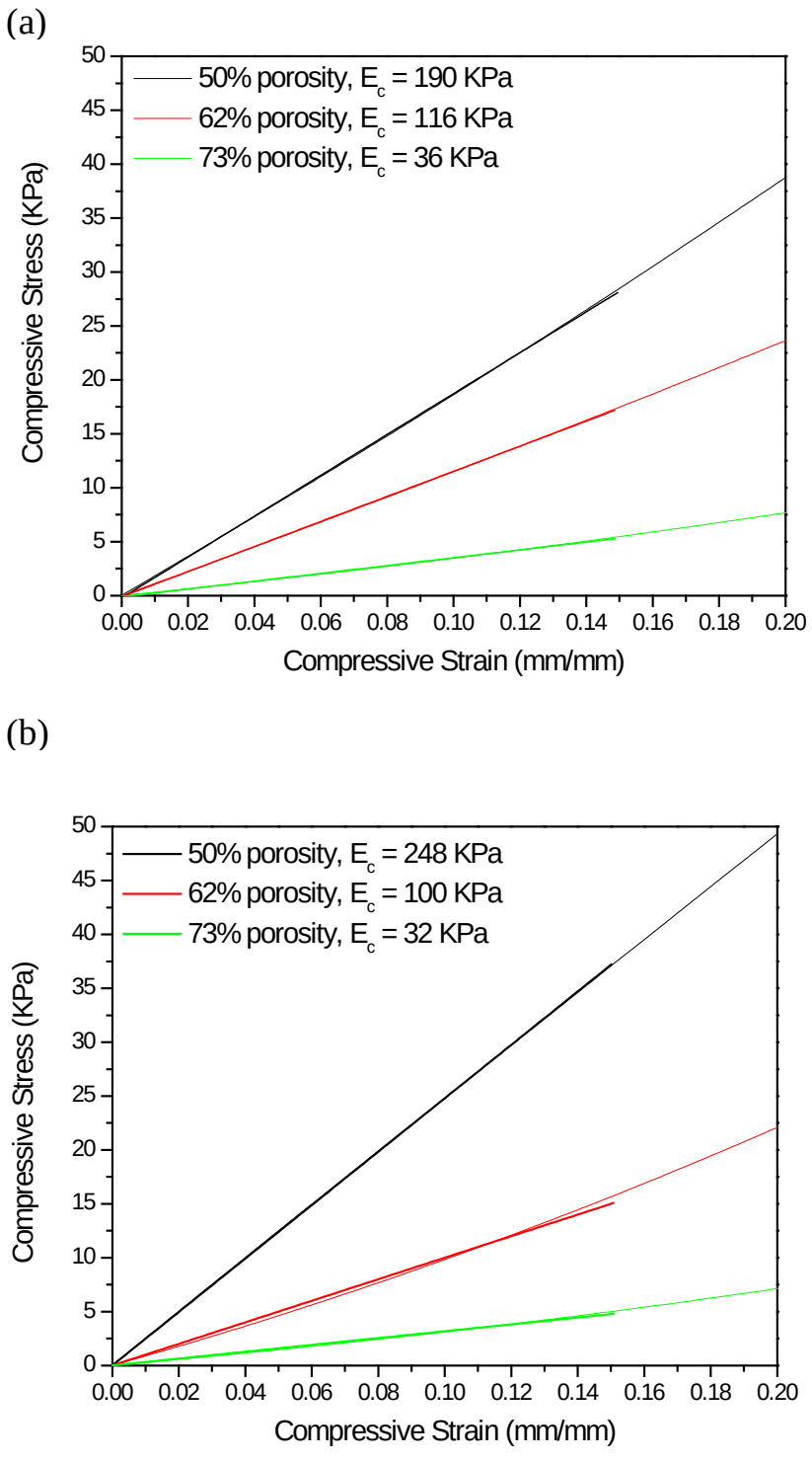

Figure 4. Compressive stress vs strain curves for (a) pure PDMS foam and (b) PNPF.

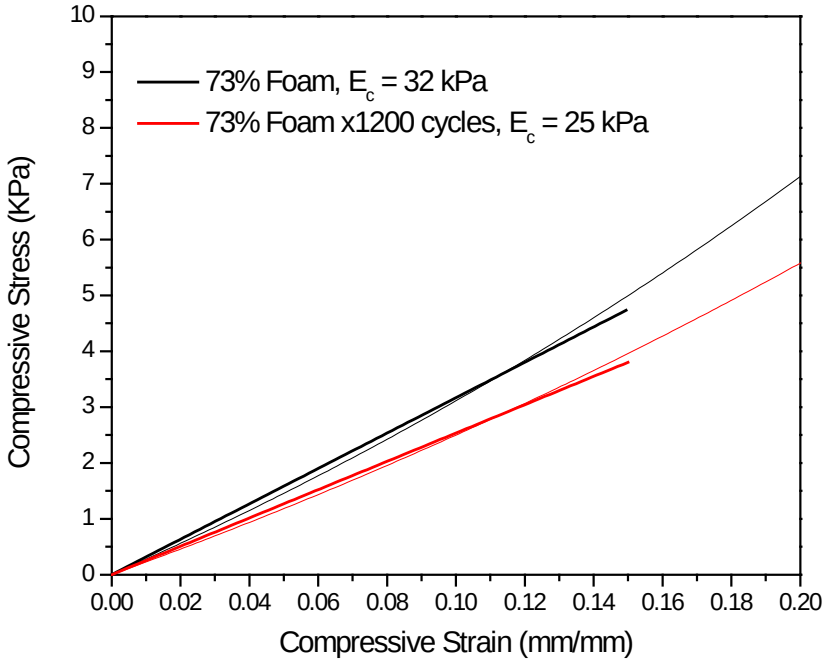

Figure 5. Cycling data of a 73% porous PNPF cube after 1200 cycles showing minimal loss to its modulus. The sample was compressed with a 10 N load at 20% strain.

1.3 Electro-mechanical Characterization of PNPFs

1.3.1 Electronic Characterization

The as-made foams are only weakly piezoelectric, or show no piezoelectric properties, since the dipoles in the BTO nanoparticles are randomly oriented. The foam materials were first activated by depositing Au/Ti (10 nm Ti followed by 200 nm of Au) on a flexible Kapton substrate and interfacing the electrodes with the top and bottom surfaces of the foam and poling on a 150°C hotplate for up to 15 hours at a field strength of > 4 V/μm to ensure a fully polarized foam (Figure 6a). By slightly compressing the ~ 300 μm films during poling, fields near the coercive field (~ 10 V/μm) could be attained

to fully polarize the BTO nanoparticles. In order to prevent dielectric breakdown during the poling process the metal electrodes were coated (via spin coating) with a thin PDMS layer (~ 5 μm) cured at 100^{o} C. After the poling was completed the electrodes were removed and replaced by a new set that had a thin layer (~ 5 μm) of the BTO/CNT composite resin to eliminate triboelectric effects. In order to create adhesion between the foams and the electrodes the surfaces were oxygen plasma treated (Harrick Plasma chamber) prior to being placed in contact. Leads were connected to the electrodes via silver epoxy (EPO-TEK® H20E, Ted Pella) and electrical wiring.

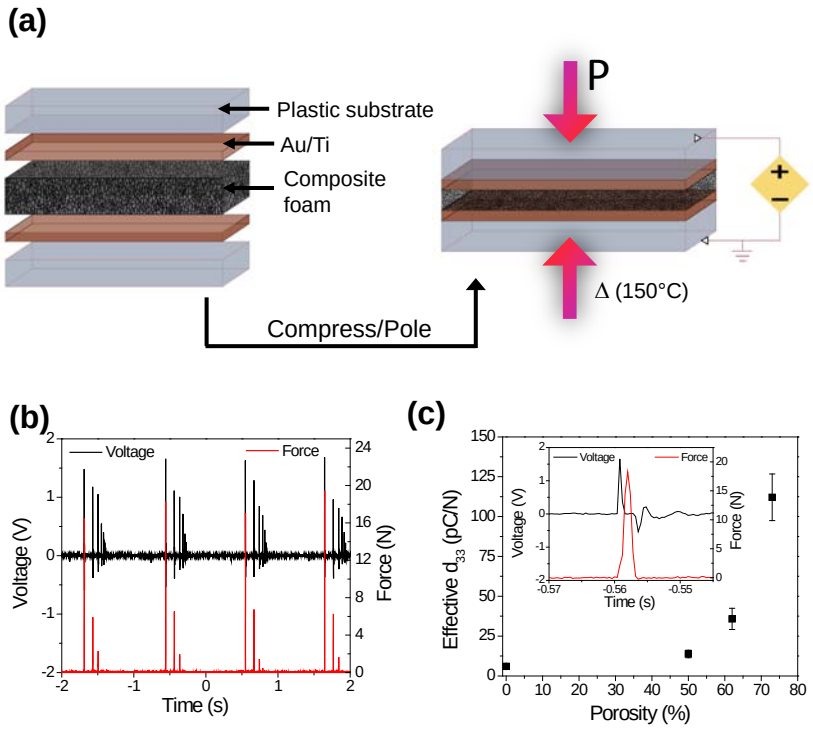

Figure 6. (a) Schematic of the poling process. Not shown are the thin (~ 5 μm) PDMS layers on the Au/Ti electrode to eliminate shorting during the poling process. To increase the poling field using a static voltage the foams can be compressed. (b) Cycling data for a 73% foam showing the piezoelectric output and applied force vs time as a rod is dropped (and allowed to bounce) on the foam 4 times. (c) Effective piezoelectric coefficient (d_{33}) of the PNPFs as a function of porosity. The neat film (0% porosity) is also shown for comparison. Data points are the average of 5 measurements and the error bars are the spread in the data. (inset) Zoom in on one of the output cycles in (b) showing the piezoelectric response of the foam as a function of time and applied force.

The piezoelectric charge coefficient (d_{33}) of the individual foams was quantified using a homemade piezoelectric test apparatus that reads out the voltage output of the material simultaneously with the applied load (Figure 7). Open circuit voltage measurements of the foams were made by stacking a device on top of a force sensor (Flexiforce®, Tekscan) with a thin square of PDMS (~ 5mm) in between. On top of the device, an identical square of PDMS was placed in contact with the top surface and covered with an aluminum sheet (~ 2 mm thick) connected to a common ground. A 21 g steel rod was dropped from a height of 5 cm and bounced on the aluminum surface to produce a signal. The lead electrode was connected to the inverting terminal of the operational amplifier and the signal was recorded by an oscilloscope (Tektronix TDS 3034). The instrument was fully calibrated using an Instron 5982 material testing apparatus and a commercial PZT film with a piezoelectric coefficient of 300 pC/N prior to testing the foams. Under the most sensitive set-up (-5 V supplied and R_1 = 10 kΩ) the sensor shows a linear relationship with respect to load above 2 N and an exponential relation below 2 N. For the experiments with the foams, a 100 pF reference capacitor and a 20 MΩ feedback resistor, R1, were used allowing the effective piezoelectic coefficient, d_{33}, to be calculated from $d_{33} = V_{out} \times 100\ pF/F_{applied}$. Figure 7b,c shows some cycling data of a 73% foam and the measured effective d_{33} values as a function of porosity. At 0% porosity (i.e., neat film) the composites show only a weak piezoelectric coefficient of 6 pC/N but by 50% porosity the value has more than doubled, eventually reaching ~ 112 pC/N at a porosity of 73%. The larger error in the piezoelectric coefficient (and strain rate in Figure 9b) at higher porosities is likely due to an increased contribution to the electrical output

from shear and/or bending modes which can slightly vary between runs when measuring a more compliant material. With only 10% loading of the BTO nanoparticles, and CNTs added to enhance the mechanical-to-electrical conversion process, these values at high porosity are significantly larger than pure polymers such as PVDF.

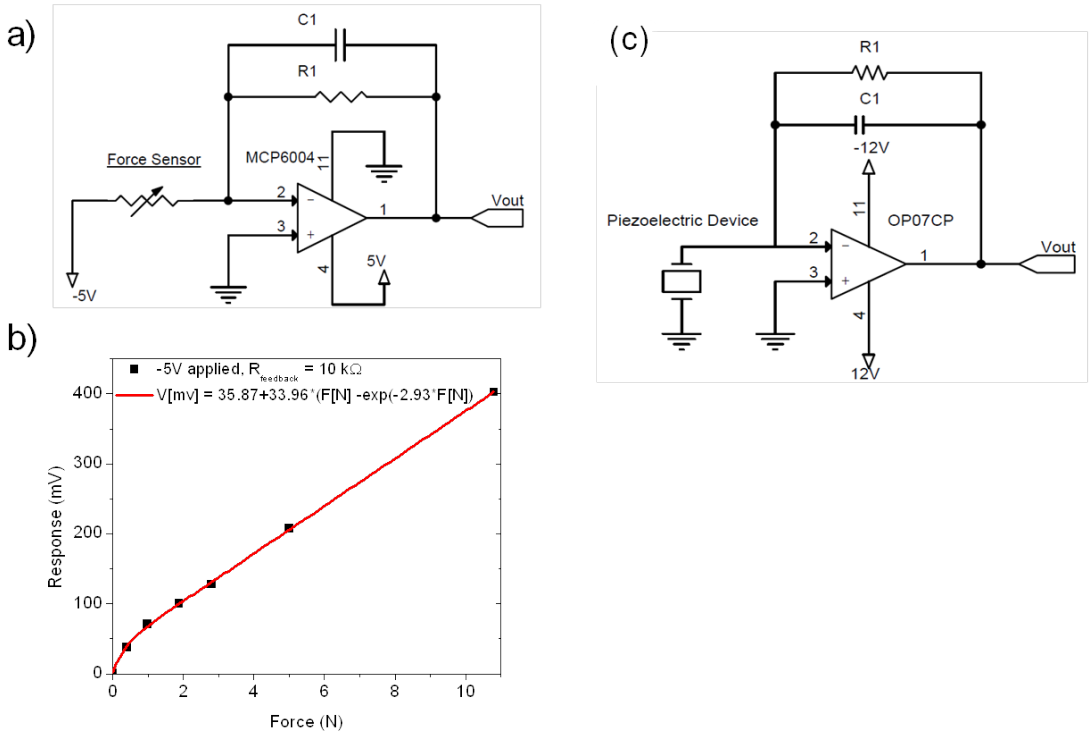

Figure 7. (a) Schematic of the FlexiForce® sensor (Tekscan) circuit that is placed underneath the foams to record the absolute force being applied to the samples simultaneously with the piezoelectric output. The output voltage of the sensor is tunable by changing the supply voltage and the feedback resistor, R_1. The capacitor, C_1, was used as the bypass capacitor. (b) Calibration curve of the force sensor. It was found that there are minimal differences between similar loads with different contact areas. (c) Schematic of the charge amplifier used in the home-build piezo-testing apparatus. Charge generated from the piezoelectric foams is transferred to the reference capacitor, C_1, which produces an output voltage, V_{out}, that is equal to the voltage across C_1 (i.e., $V_c = -Q_{generated}/C_1$).

We believe the enhanced piezoelectric properties of the foam structure are due to a combination of effects which include being a softer material (i.e., smaller loads required to strain the material) compared to the 0% films and that the interconnected polymer

matrix is helping to localize stresses on the piezoelectric nanoparticles. To boost the piezoelectric output further, various strategies can be employed such as direct grafting of the BTO nanoparticles to the polymer chains,[17] using piezoelectric nanoparticles with higher intrinsic d_{33} values (e.g., PZT), or increasing the nanoparticle loading percent.

1.3.2 Decoupling the Triboelectric Effect

It is important when dealing with high surface area materials to properly decouple the piezoelectric effects from other charge forming processes such as the triboelectric effect. It has been shown that when materials (e.g., polymers) with different contact charging properties are interfaced, they can produce large static-charge driven signals while in physical contact.[24] This triboelectric effect is even further enhanced when two materials at different regions of the tribo-series are roughened and then brought together.[25] Similar to a reduction-oxidation potential, the further the materials are away from each other on a triboelectric scale, the larger the electrostatic potentials will be when the two materials come in contact. It is expected that there will be strong triboelectric effects for devices that contain a high surface area PDMS foam in contact with an electrode. We investigated this and found that the pure PDMS foams produced recordable triboelectric responses when a load is applied to the foam (Figure 8). Three devices were fabricated using either a thin (~ 5 μm) PDMS layer or composite resin on the electrodes and then interfaced with the pure PDMS or composite foam. To ensure that the recorded voltages were purely due to the triboelectric effect, the foam samples were not subjected to poling fields. Each data set shows a drop test where an ~ 10 N load was dropped on the device and allowed to bounce sequentially on the surface.

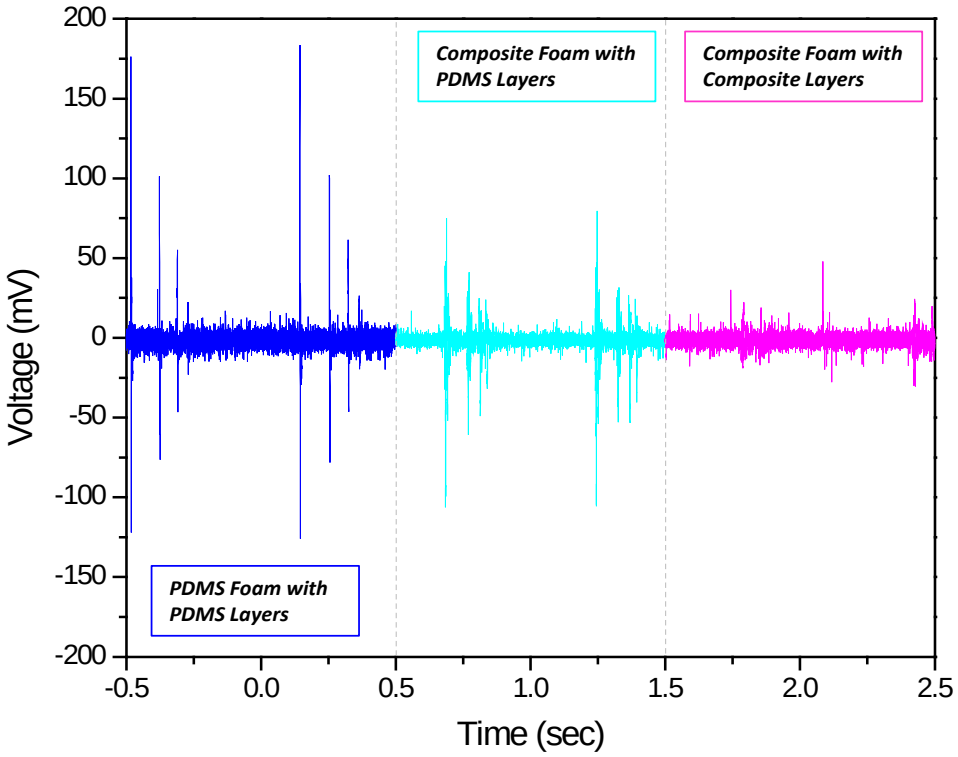

Figure 8. Plots showing the electrical response of various electrode/sample interfaces to understand the effects of contact, or static, charge generation (i.e., triboelectric effect). By using the composite resins on the electrodes, instead of pure PDMS, it was found that the static charges could be eliminated which allowed us to decouple the piezoelectric and triboelectric effects.

When the unpoled piezoelectric composite foams were tested with pure PDMS coatings on the electrodes there were still measureable static potentials. However, the triboelectric effect could be suppressed by first poling with the pure PDMS coatings and then switching to unpoled composite layers (~ 5 μm thick) on the electrodes. This minimizes

the difference on the tribo-scale and allowed the piezoelectric properties to be probed independently from contact charging effects.

1.3.3 PNPF Charge Dynamics

With such large surface-to-volume ratios, it is likely that the charging dynamics of the foams will be different depending on the porosity. To investigate this we tracked both the applied force and voltage output of the foam in real-time. Figure 9a captures single charging and discharging cycle for a neat film and samples with different porosity. As force is applied to the foam, the material is compressed which strains the BTO nanoparticles, causing a recordable piezoelectric potential across the foam. For an ideal piezoelectric material (i.e., one that can efficiently hold charge over time) the voltage should peak at max force, but if charge is lost too quickly there will be an offset between the max voltage and max force. This can be clearly seen with the foams when plotting the time difference (Δt), defined as the time delay between when the max voltage and force are recorded, as a function of porosity (Figure 9b). Before the maximum force is attained, the porous materials have already lost most of their charge. This suggests that the PNPFs are poor capacitors and that we could be underestimating the piezoelectric coefficients for our materials. To get smaller Δt values, higher strain rates need to be used but under the current loading experiments, we are only able to attain strain rates of up to ~ 10 s^{-1}. Strain rate values were calculated from the equation[26]:

$$i = q/t = d_{33}E_cA(\varepsilon/t)$$

where i is the current generated by the material, d_{33} is the piezoelectric charge coefficient, E_c is the modulus, A is the active area, and ε/t is the strain rate. Dividing the current by the charge coefficient yields the force per unit time, F/t. We can then solve for strain rate:

$$\varepsilon/t = (F/t)/[E_c A]$$

The values of *(F/t)* were calculated by taking the slope of each force curve produced during the piezoelectric testing.

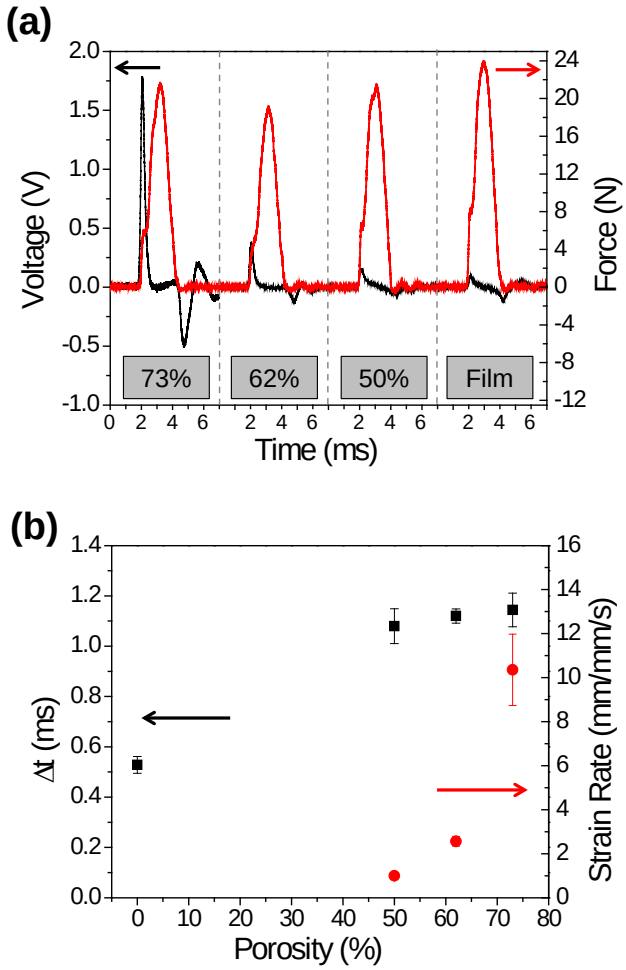

Figure 9. (a) Single charge/discharge traces (7 ms each) for a 0% (neat film), 50%, 62%, and 73% porous film. The applied force is also plotted in real–time. (b) Time difference between peak voltage and force as a function of porosity. Also plotted is the compressive strain rate of the foam as a function of porosity under an ~ 10 N load.

Future work will investigate how strain rate and frequency can be used to tune the piezoelectric response of the PNPFs and we will explore ways of improving electrical capacitance of the porous materials (e.g., different electrodes, foam passivation layers, etc.). A closer look at the foam cycling curves also supports the claim of a charging/discharging process that is strongly dependent on the strain rate. For the neat film, there exists a predominant charge and discharge trace that has much better symmetry compared to the porous films. This is due to the similar strain rates during compression and recovery. However, for the foams, the charge cycle peaks at a much larger value compared to the discharge. This can be explained by the slow elastic recovery of the foam materials after compression which results in a much smaller strain rate and weaker discharge signal.

1.3.4 PNPF Power Generation

Power transfer from a device connected to an external load was measured by recording the voltage across a potentiometer in series with the device (1kΩ, 200kΩ, 1MΩ) according to:

$$P_T = V^2/R_{pot}$$

where P_T, V, and R_{pot} is the power, voltage across the potentiometer, and resistance of the potentiometer, respectively. The power density was calculated by taking the ratio of power transferred over the volume of active material in the device:

$$P_D = P_T/[\pi * r_f^2 * t * \varphi_i]$$

where r_f is the radius (~ 5 mm) of the active area, t is the thickness ($300 < t < 400$ μm) of the foam, and φ_i is the volume fraction of the foam, respectively. All electrical measurements were taken 5 times and the displayed data (Figure 6c and Figure 9b) shows

the average value along with the spread of the data (error bar). The foams were cycled with ~ 10 N loads and the resulting power densities are plotted in Figure 10a. Under small external loads we see the lowest power output, but once the load is increased to values above ~ 10 kΩ the power density steadily climbs to ~ 18 mW/cm^3 for the highest porosity samples and then plateaus. This trend fits the electronic model of an ideal capacitor which has infinite impedance. In order to maximize power transfer from the piezoelectric device to a load resistor the impedances of both must be matched. Since the foams are essentially high impedance, parallel plate capactitors with air as the dielectric, it is expected that the foams will produce the highest power densities under higher electrical loads. In addition to measuring the power output under varying external loads, the ability of the PNPFs in charging up a capacitor were investigated. The device was connected to a simple rectifying circuit, which included a 100 nF charging capacitor, and subjected to a cycling load of ~ 8 N at 118 Hz. The voltage across the capacitor, and the impulse train, were recorded with time (Figure 10b) and showed a maximum voltage of ~175 mV after ~ 200 ms. Due to the quick charging and discharging capability of the device it is expected that higher frequency stimuli under smaller loads will produce faster capacitor charging times and larger voltages.

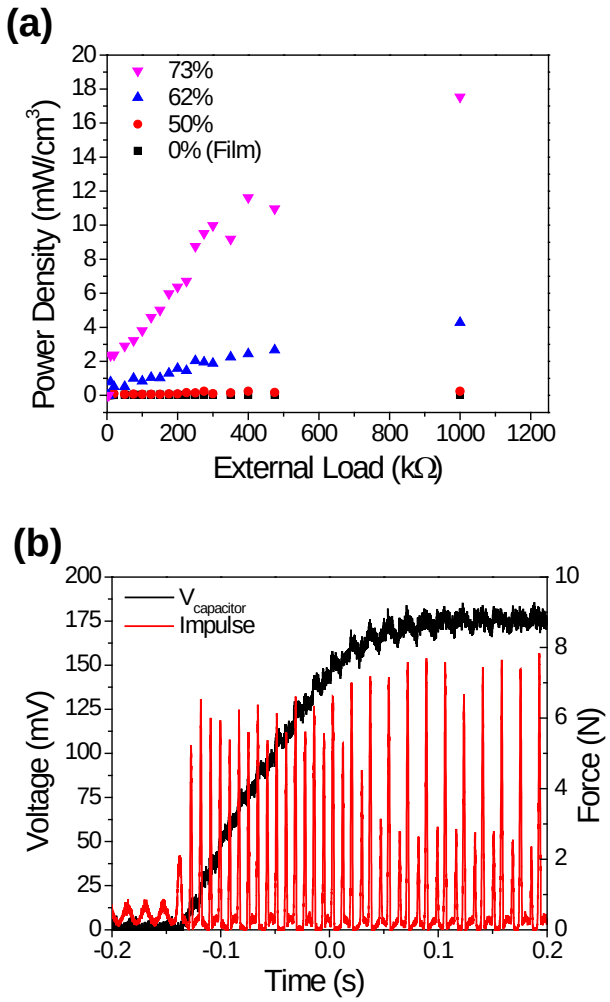

Figure 10. (a) Power output as a function of external load for different porosity films and a neat film. A ~ 10 N load is being applied to the samples. (b) Plot showing the charging up of a 100 nF capacitor. The voltage and 118 Hz impulse force are plotted as a function of time.

1.4 Conclusions

In summary we have utilized simple sugar-templating methods to fabricate piezoelectric polymer composite foams. Two strategies were laid out for creating porous piezoelectric polymers including a capillary-action and roll-out method. The roll-out process allowed much finer control over the porosity, enabled much thinner films, and has the potential to be scaled up to fabricate material over large areas. The mechanical studies showed the anticipated trend of lower elastic coefficients at higher porosity whereas the piezoelectric properties were signicantly boosted when the air fraction was increased. Due to the the large surface area of the foams, it was observed that charge across the foam could not be held as efficiently as the thin films, but created a much more sensitive material. Improvements on the capacitance and discharging dynamics of the foams should be attainable by leveraging different electrode interfaces, passivating layers, and/or composite materials that eliminate the CNTs. Power studies indicated that these materials can operate under mechanical loads and have enough power to drive low power devices. Given the tunable porosity, mechanical flexibility of the foams, high surface area, high piezoelectric sensitivity, isotropic microscture, and more biocompatible chemical make-up compared to the bulk electroceramic counterparts, these foams should find immediate applications in energy scavenging platforms, biosensors, and acoustic transducers.

Chapter 1, in full, is a reprint of the material as it appears in ACS Applied Materials & Interfaces 2014. W.R. McCall was the primary investigator and author of this paper.

1.5 References

1 Allahverdi, M.; Danforth, S. C.; Jafari, M.; Safari, A. Processing of Advanced Electroceramic Components by Fused Deposition Technique. *J. Eur. Ceram. Soc.* **2001,** *21*, 1485-1490.

2 Tuttle, B. A.; Smay, J. E.; Cesarano, J.; Voigt, J. A.; Scofield, T. W.; Olson, W. R.; Lewis, J. A. Robocast $Pb(Zr_{0.95}Ti_{0.05})O_3$ Ceramic Monoliths and Composites. *J. Am. Ceram. Soc.* **2001,** *84*, 872-874.

3 Rittenmyer, K.; Shrout, T.; Schulze, W. A.; Newnham, R. E. Piezoelectric 3-3 Composites. *Ferroelectrics* **1982,** *41*, 189-95.

4 Kara, H.; Ramesh, R.; Stevens, R.; Bowen, C. R. Porous PZT Ceramics for Receiving Transducers. *IEEE Trans. Ultrason. Eng.* **2003,** *50*, 289-296.

5 Bast, U.; Wersing, W. The Influence of Internal Voids with 3-1 Connectivity on the Properties of Piezoelectric Ceramics Prepared by a New Planar Process. *Ferroelectrics* **1989,** *94*, 229-242.

6 Boumchedda, K.; Hamadi, M.; Fantozzi, G. Properties of a Hydrophone Produced with Porous PZT Ceramic. *J. Eur. Ceram. Soc.* **2007,** *27*, 4169-4171.

7 Kawai, H. Piezoelectricity of Poly (Vinylidene Fluoride). *Jpn. J. Appl. Phys.* **1969,** *8*, 975-976.

8 Hu, Z.; Tian, M.; Nysten, B.; Jonas, A. M. Regular Arrays of Highly Ordered Ferroelectric Polymer Nanostructures for Non-Volatile Low-Voltage Memories. *Nat. Mater.* **2009,** *8*, 62-67.

9 Foster, F. S.; Harasiewicz, E. A.; Sherar, M. D. A History of Medical and Biological Imaging with Polyvinylidene Fluoride (PVDF) Transducers. *IEEE Trans. Ultrason. Eng.* **2000,** *47*, 1363-1371.

10 Harris, G. R.; Preston, R. C.; DeReggi, A. S. The Impact of Piezoelectric PVDF on Medical Ultrasound Exposure Measurements, Standards, and Regulations. *IEEE Trans. Ultrason.. Eng.* **2000,** *47*, 1321-1335.

11 Wang, F.; Tanaka, M.; Chonan, S. Development of a PVDF Piezopolymer Sensor for Unconstrained in-Sleep Cardiorespiratory Monitoring. *J. Intell. Mater. Syst. Struct.* **2003,** *14*, 185-190.

12 Chang, C. E.; Tran, V. H.; Wang, J. B.; Fuh, Y. K.; Lin, L. W. Direct-Write Piezoelectric Polymeric Nanogenerator with High Energy Conversion Efficiency. *Nano Lett.* **2010,** *10*, 726-731.

13 Hansen, B. J.; Liu, Y.; Yang, R. S.; Wang, Z. L. Hybrid Nanogenerator for Concurrently Harvesting Biomechanical and Biochemical Energy. *ACS Nano* **2010,** *4*, 3647-3652.

14 Persano, L.; Dagdeviren, C.; Su, Y.; Zhang, Y.; Girardo, S.; Pisignano, D.; Huang, Y.; Rogers, J. A. High Performance Piezoelectric Devices Based on Aligned Arrays of Nanofibers of Poly(Vinylidenefluoride-Co-Trifluoroethylene). *Nat. Commun.* **2013,** *4*, 1-10.

15 Cha, S.; Kim, S. M.; Kim, H.; Ku, J.; Sohn, J. I.; Park, Y. J.; Song, B. G.; Jung, M. H.; Lee, E. K.; Choi, B. L.; Park, J. J.; Wang, Z. L.; Kim, J. M.; Kim, K. Porous PVDF as Effective Sonic Wave Driven Nanogenerators. *Nano Lett.* **2011,** *11*, 5142-5147.

16 Park, K.-I.; Lee, M.; Liu, Y.; Moon, S.; Hwang, G.-T.; Zhu, G.; Kim, J. E.; Kim, S. O.; Kim, D. K.; Wang, Z. L.; Lee, K. J. Flexible Nanocomposite Generator Made of $BaTiO_3$ Nanoparticles and Graphitic Carbons. *Adv. Mater.* **2012,** *24*, 2999-3004.

17 Kim, K.; Zhu, W.; Qu, X.; Aaronson, C.; McCall, W. R.; Chen, S. C.; Sirbuly, D. J. 3D Optical Printing of Piezoelectric Nanoparticle-Polymer Composite Materials. *ACS Nano* **2014,** *DOI: 10.1021/nn503268f*.

18 Park, I.; Efimenko, K.; Sjoblom, J.; Genzer, J. Rapid Removal of Organics and Oil Spills from Waters Using Silicone Rubber "Sponges". *J. Dispersion Sci. Technol.* **2009,** *30*, 318-327.

19 Choi, S. J.; Kwon, T. H.; Im, H.; Moon, D. I.; Baek, D. J.; Seol, M. L.; Duarte, J. P.; Choi, Y. K. A Polydimethylsiloxane (Pdms) Sponge for the Selective Absorption of Oil from Water. *ACS Appl. Mater. Interfaces* **2011,** *3*, 4552-4556.

20 Zhang, A. J.; Chen, M. J.; Du, C.; Guo, H. Z.; Bai, H.; Li, L. Poly(Dimethylsiloxane) Oil Absorbent with a Three-Dimensionally Interconnected Porous Structure and Swellable Skeleton. *ACS Appl. Mater. Interfaces* **2013,** *5*, 10201-10206.

21 Lee, H.-W.; Moon, S.; Choi, C.-H; Kim, D. K. Synthesis and Size Control of Tetragonal Barium Titanate Nanopowders by Facile Solvothermal Method. *J. Am. Ceram. Soc.* **2012,** *95*, 2429-2434.

22 Evan, H. T. An X-ray diffraction study of tetragonal barium titanate. *Acta Cryst.* **1961,** *14*, 1019-1026.

23 Peng, S.; Hartley, P. G.; Hughes, T. C.; Guo, Q. Controlling Morphology and Porosity of Porous Siloxane Membranes through Water Content of Precursor Microemulsion. *Soft Matter* **2012,** *8*, 10493-10501.

24 Diaz, A. F.; Felix-Navarro, R. M. A Semi-Quantitative Tribo-Electric Series for Polymeric Materials: The Influence of Chemical Structure and Properties. *J. Electrostatics* **2004,** *62*, 277-290.

25 Fan, F.-R.; Lin, L.; Zhu, G.; Wu, W.; Zhang, R.; Wang, Z. L. Transparent Triboelectric Nanogenerators and Self-Powered Pressure Sensors Based on Micropatterned Plastic Films. *Nano Lett.* **2012,** *12*, 3109-3114.

26 Sirohi, J.; Chopra, I. Fundamental Understanding of Piezoelectric Strain Sensors. *J. Intell. Mater. Sys. Struct.* **2000,** *11*, 246-257.

2 3D Optical Printing of Piezoelectric Nanoparticle-Polymer Composite Materials

*ACS Nano 2014

2.1 Introduction

The ability to convert compressive/tensile stresses to an electric charge, or vice versa, has long been an intriguing and valuable property of piezoelectrics. Applications that utilize the direct (mechanical stress forming an electric field) or converse (electric voltage forming a mechanical deformation) piezoelectric effect are far reaching ranging from loud speakers and acoustic imaging to energy harvesting and electrical actuators. Most piezoelectric materials in systems are based on brittle ceramics such as lead zirconate titanate (PZT) which has one of the highest known piezoelectric coefficients (d_{33} > 300 pC/N; depending on composite and processing conditions).[1] Although much smaller piezoelectric responses compared to PZT, $Pb(Mg_{1/3}Nb_{2/3})O_3$-$PbTiO_3$ (PMN-PT; d_{33} up to ~ 2500 pC/N),[2] or other perovskite-based oxides such as barium titanate ($BaTiO_3$ – BTO; d_{33} > 200 pC/N; depending on ceramic type and processing conditions)[3-5], piezoelectric polymer materials offer several unique capabilities that make them ideal candidates for systems that require mechanical flexibility, smaller active elements, biocompatibility, and processability. One of the most widely studied pure polymers in this group is polyvinylidene fluoride (PVDF), discovered in 1969 by Kawai,[6] which has a piezoelectric coefficient (d_{33} ~ -20 to -34 pC/N) that is over an order of magnitude smaller than PZT. Due to its excellent mechanical flexibility, biocompatibility, and solution-based processability it is actively being investigated for applications including non-volatile low voltage memory,[7] acoustic transducers,[8-9] and implantable medical

devices.[10-11] PVDF materials are some of the best standards when it comes to piezoelectric polymer performance, yet it is difficult to fabricate these structures into individual active elements, complex architectures, or 3-dimensional (3D) patterns. Breakthroughs in the area of micro- and nanofabrication of piezoelectric polymers will have an enormous impact on the development of biodiagnostics, nano- and microelectromechanical systems (NEMS/MEMS), imaging, sensors, and electronics.

There are many nano- and microfabrication techniques available for ferroelectric and piezoelectric materials including electron beam lithography,[12-13] ion milling,[14-15] soft lithography,[16] self-assembly,[17]electrospinning,[18] and contact printing.[19] However, these techniques do not offer simple approaches to fabricating 3D structures in piezoelectric polymers or multilayered architectures which would open up infinite possibilities in the design of more complicated device geometries. To address the 3D printing aspect of active piezoelectric materials and pursue low-cost fabrication approaches for producing high-fidelity patterns and structures over large areas, we investigated stereolithographic (SLA) methods that use photoliable piezoelectric polymer composite materials. The general procedure for building 3D structures with SLA involves the exposure of light (typically from a laser or light emitting diode) to a photoliable liquid (e.g., polymer solution with acrylated monomer units) which creates cross-linked regions where the light irradiates the matrix. Once a single layer is carved out with the light, the sample is translated to allow the next layer to be written. The actual patterning can be programmed with Computer-Aided Design (CAD) but resolution is limited by actinic radiation, free radical diffusion, and the optical system which is typically ~ 75 to 250 μm in the x-y direction and about 100 μm in the z-direction.[20] The throughput of the SLA process is

also slow due to the point-by-point scanning nature of the direct-write. To achieve higher throughput and resolutions using the basic concepts of SLA, microscale digital projection printing (DPP) can be used which leverages a digital micromirror-array device (DMD) to produce a dynamic digital mask.[21-22] The projected images from the DMD are focused on the polymer solution and feature sizes as small as 1 μm can be generated by sequential polymerization steps.[23]

In this work we describe how DPP can be utilized to photopolymerize piezoelectric nanoparticle-polymer colloidal suspensions into user-defined 2D or 3D structures in mere seconds. The piezoelectric nanoparticles are chemically modified with photosensitive surface groups and incorporated into photoliable polymer solutions. Under light exposure, the polymer cross-links with the chemical groups on the piezoelectric nanoparticles which grafts the nanoparticles to the polymer backbones. This direct linkage to the flexible polymer matrix enhances the piezoelectric output of the composite films by efficiently funneling mechanical stress to the piezoelectric crystals. A significant boost in the piezoelectric coefficient is observed for the chemically modified nanoparticles compared to other composites with similar polymer matrices infused with carbon nanotube fillers and unmodified nanoparticles or unmodified nanoparticles alone. These results provide an immediate solution to fabricating 3D piezoelectric materials and uncover a novel strategy to enhance mechanical-to-electrical conversion in nanocomposites.

2.2 Materials Synthesis and Photofabrication Process

2.2.1 Preparation of PEGDA and BTO Nanoparticle Composites

To produce 3D photo-writable piezoelectric polymers we focused on composite materials that could easily incorporate piezoelectric nanoparticles into a photoliable polymer solution. After defining a digital mask, the polymer solution can then be exposed to pattern of light (Figure 11a) and the liquid polymerizes and encapsulates the piezoelectric nanoparticles. The system we chose for the initial work leverages BTO nanoparticles embedded in a polyethylene glycol diacrylate (PEGDA) matrix, but the platform should be universal for other photoliable polymers [e.g., poly(methyl methacrylate), poly(acrylic acid), poly(lactic acid)] and piezoelectric materials (e.g., PZT, ZnO, PMN-PT, $NaNbO_3$). The BTO nanoparticles were synthesized using well-known hydrothermal processing that combines metal alkoxides such as Ti-butoxide ($Ti[O(CH_2)_3CH_3]_4$ with metal hydroxides such as $Ba(OH)_2$ in an autoclave at 150 – 300 °C.[24] The mean diameter of the synthesized nanoparticles was 85 ± 15 nm (Figure 11b). To enhance the stress transfer efficiency from the matrix to the BTO nanoparticles and boost the piezoelectric outputs of the fabricated materials, a 3-trimethoxysilylpropyl methacrylate (TMSPM) linker molecule was used to covalently graft the BTO surface to the PEGDA matrix (Figure 11c). Prior to mixing the BTO nanoparticles with the polyethylene glycol diacrylate (PEGDA) solutions, the dried nanoparticles were functionalized with 3-trimethoxysilylpropyl methacrylate (TMSPM) using similar grafting strategies to those carried out on silica surfaces.[30] The TMSPM solution consisted of 1 mL TMSPM dissolved in 50 mL of ethanol and mixed with an acetic acid solution (1 mL acetic acid in 9 mL of DI water). The BTO nanoparticles (~ 6 g) were

then added to the TMSPM solution and sonicated for 24 hours. After the surface functionalization step, the particles were cleaned with copious amounts of ethanol and water and dried.

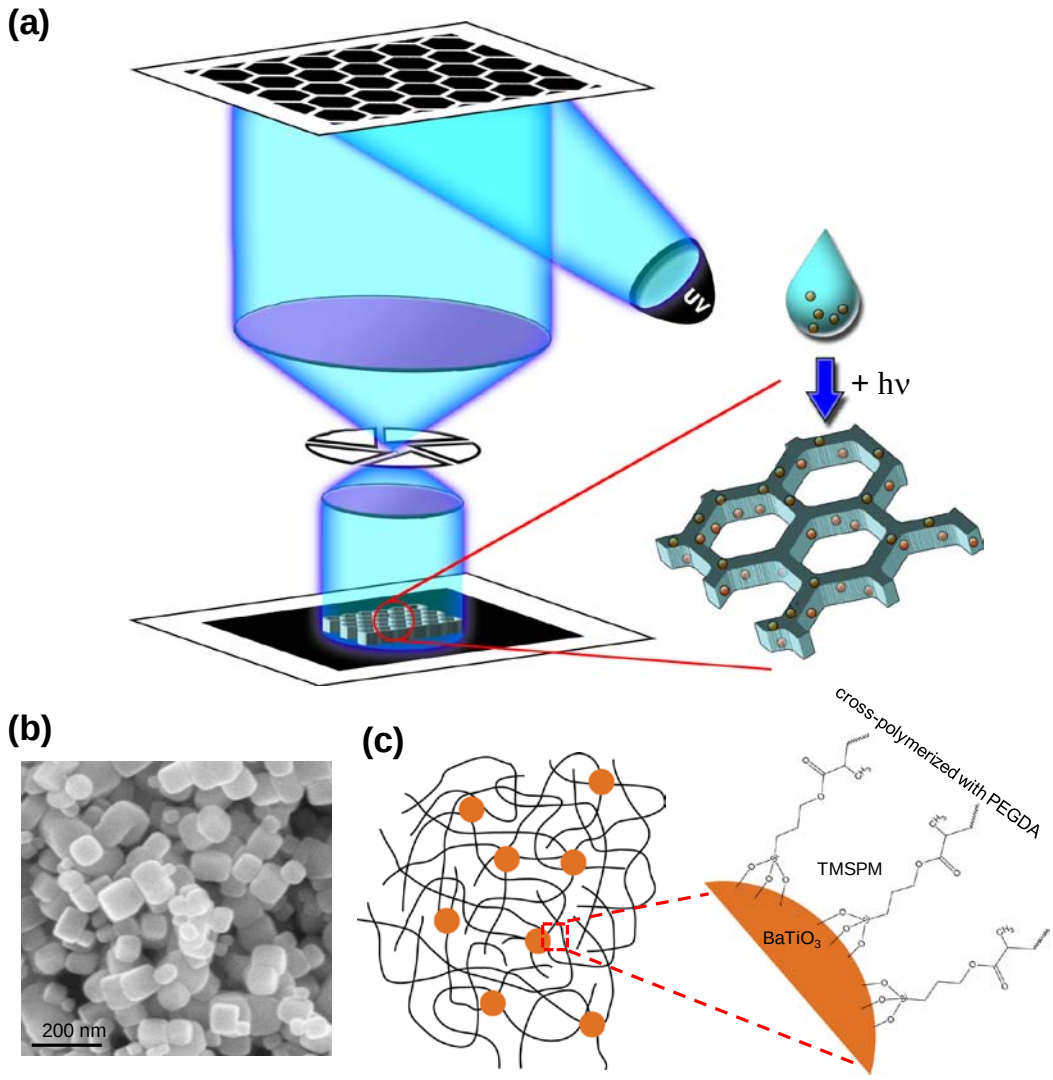

Figure 11. (a) Schematic of the DPP setup that projects dynamic digital masks on the photoliable piezoelectric nanoparticle-polymer composite solution. Any pattern can be digitized and the digital mirror device projects the image onto the polymer solution. (b) Scanning electron micrograph of BTO nanoparticles grown via a hydrothermal process. (c) Cartoon showing the piezoelectric polymer composite materials with BTO nanoparticles (orange circles) grafted to a PEGDA matrix (black lines). The zoom in shows the TMSPM linker covalently linked to the nanoparticle surface and cross-linked with the PEGDA matrix.

2.2.2 FTIR of TMSPM-grafted BTO Nanoparticles

FTIR measurements were taken on as-made and freshly functionalized nanoparticles (Figure 12). To prepare the BTO-loaded PEGDA solutions, appropriate BTO:PEGDA weight ratios were used to achieve the desired mass loading and the samples were sonicated for > 24 hours prior to photopolymerization.

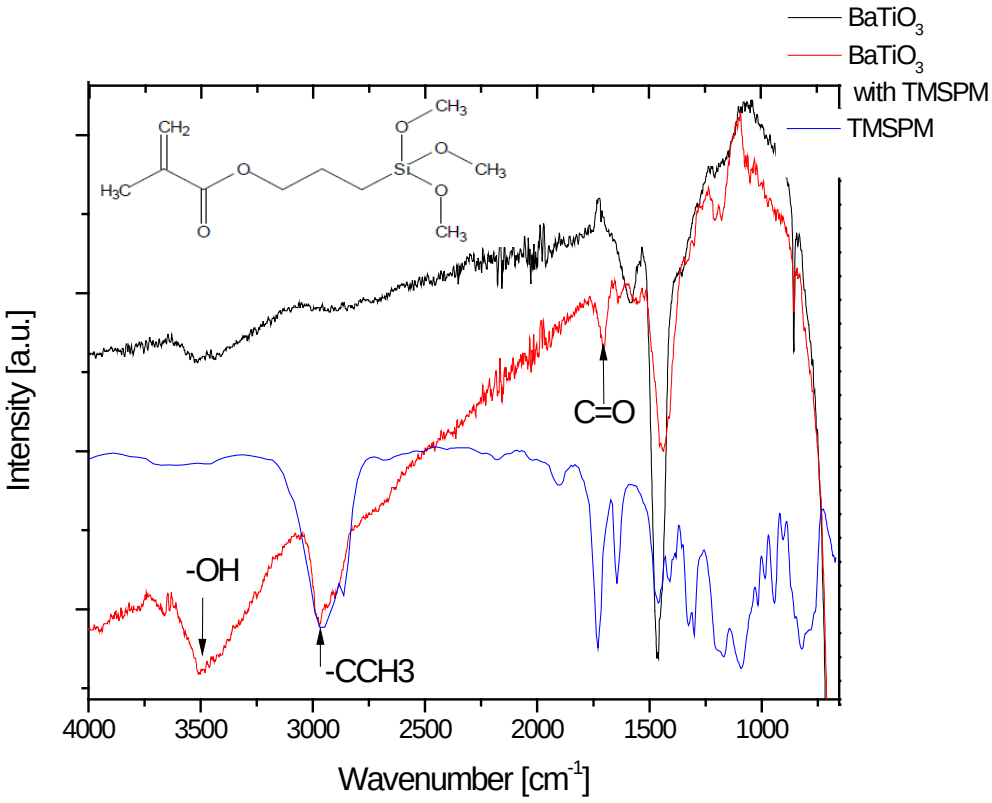

Figure 12. The chemical structure of TMSPM (top left) and FTIR spectra of pure TMSPM (blue), as-made BTO nanoparticles (black), and TMSPM-grafted BTO nanoparticles (red). The bands at 2862-2882 cm^{-1} are attributed to C-CH_3 and O-CH_3 groups and the band at 1720 cm^{-1} is attributed to the C=O group. The broad peak centered at 3500 cm^{-1} is attributed to hydroxyl groups on the BTO nanoparticles which are present both in the as-made and TMSPM-modified samples. The samples were washed with copious amounts of ethanol and water prior to taking spectra and provide good evidence (along with the enhanced piezoelectric properties) that the TMSPM is grafted to the surface of the BTO nanoparticles. The spectra were recorded using a Spectrum Two spectrometer (Perkin Elmer).

2.2.3 Optical Printing and Film Preparation

The optical printing cells consisted of cover glass slides coated with 100 nm of ITO deposited by magnetic sputtering. The electrodes were covered with ~1 μm of polymethyl methacrylate (PMMA) to prevent shorting. A photoinitiator such as 2,2-dimethoxy-2-phenylacetophenone (DMPA) or 2,2-dimethoxy-1,2-di(phenyl)ethanone (Irgacure 651) was added to the PEGDA composites at a concentration of 1 wt %. The PEGDA composite was then placed between the two electrodes using a 25 μm Kapton film spacer and the polymer could be polymerized using 365 nm light from an LED (for DPP) or a hand held UV lamp (for film preparation). The power of the hand held lamp was much lower than the LED which required longer exposure times (minutes) to photopolymerize. Electrical wires were connected to the electrodes using silver epoxy and the photopolymerized samples were electrically poled at a field of ~ 12 MV/m at 120 °C for 24 hours. The piezoelectric properties of the polymers were characterized using a home-built charge amplifier and a commercially available force sensor (Chapter 1, Figure 6). The piezoelectric polymer was placed in between two PDMS pieces prior to placing on the force sensor to protect the materials during the mechanical test and to distribute the load equally over the active area of the piezoelectric. Under light exposure the carbon-carbon double bonds of the TMSPM cross-link with the polymer matrix forming a strong bond between the piezoelectric nanoparticles and polymer network. Compared to other piezoelectric composite materials that utilize BTO nanoparticles embedded in an elastomer [e.g. polydimethylsiloxane (PDMS)], with carbon nanotubes (CNTs) as a mechanical-to-electrical enhancer,[25] the direct grafting of molecular linkers provides a

simpler and more efficient route to help funnel energy to the piezoelectric structures. In addition, removing the CNTs significantly improves the optical transparency of the material. Other nanocomposite polymers have been demonstrated to produce strong piezoelectric outputs without the need for additives (e.g., PDMS/PMN-PT nanowire composites),[26] but these utilize nanomaterials with higher intrinsic piezoelectric performance. After mixing the surface-treated BTO nanoparticles with the PEGDA solution, a photoinitiator such as 2,2-dimethoxy-2-phenylacetophenone(DMPA) or Irgacure 651 is added to generate free radicals in regions exposed to light. Once free radicals are formed they attack the C=C bonds of the monomers in solution, producing acrylic monomers with free electrons that attack other monomers forming oligomers and eventually a vast cross-linked network. The chain reaction propagates until two radicals neutralize or the irradiation source is turned off. For our DPP set-up, the microstructure arrays were fabricated in very short times (< 2 seconds), and this can be further tuned by altering irradiation power, photoinitiator concentration, monomer concentration, nanoparticle loading, and/or adding a quencher.

2.3 Photofabrication Results

2.3.1 2D Structures

With superb control over the digital photomask, virtually any shape can be projected onto the polymer solution and printed within seconds. Figure 13 shows a collage of different microstructures, including dot, square, and honeycomb arrays that were fabricated using a custom built DPP apparatus coupled with a 365 nm light emitting diode (LED) light source. Although similar structures can be produced with other fabrication methods such as contact printing, the photo-printing process can be carried

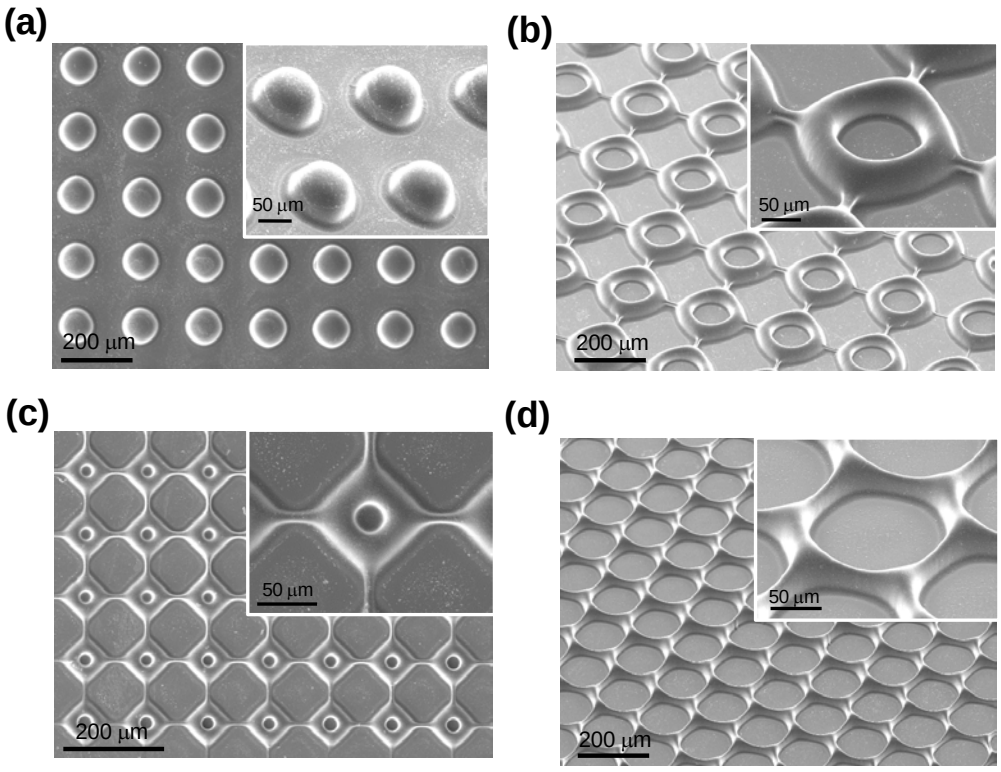

Figure 13. Collage of piezoelectric microstructures printed using DPP including a (a) dot array, (b-c) square arrays with different sized void spaces, and (d) a honeycomb array. All structures were fabricated in < 2 seconds using a PEGDA solution loaded with 1 % of the TMSPM-modified BTO nanoparticles.

out over very larger areas with high reproducibility and fidelity. In addition, there is low instrumental complexity and the fabrication time to create batch arrays with different geometric shapes and structures can be orders of magnitude faster than techniques that require a separate mask processing step.

2.3.2 3D Structures

For 3D direct printing the stage can be translated in the z-direction (perpendicular to substrate surface) while the projected image is altered. By focusing the projected light on a plane in the liquid (or liquid surface), and synchronizing the stage movement with the incremental change in the projected features, 3D structures can be carved out with

smooth side walls using a process called dynamic optical projection stereolithography (DOPsL).[27] Figure 14a-c shows various 3D structures created using this approach including an arbitrary mushroom-like array that has a smaller base diameter compared to the top, a cross array with a recessed center and rounded edges, and a tapered cantilever array. To create structures with complex void regions that are layered on top of each other, or features that are hollowed out, will require more sophisticated photopolymerization techniques. The structures and arrays fabricated in Figures 13 and 14 rely on single photon absorption events to catalyze the cross-linking process. This limits how deep/thick a 2D structure is since light will be absorbed in the top layer, thereby creating free radicals well above the focal area underneath. To minimize overexposure to regions outside the focal plane optical quenchers can be used to lower the rate of free radical formation, but the depth is still limited by attenuation of the digital mask. This can be circumvented by using DOPsL to fabricate 3D structures since the process can be designed to only photopolymerize on the top surface of the liquid. New polymer solutions can either be flown into the reaction cell while the vertical stage is manipulated or the polymerization can be done in sequential steps without ever having to project the digital mask through thicker (> 5 μm) unpolymerized layers.

The 2D and 3D patterns demonstrate the ability to reach a resolution limit of ~ 5 μm with curved, adjoining, straight, and/or void regions (e.g., see zoom-in images in Figure 14b-c) which is close to the limit of DPP (~ 1 μm) for pure polymers. The resolution is strongly dependent on the light-matter interaction of the BTO nanoparticles. We found that BTO mass loadings of 1 – 10 % and 1 % photoinitiator produced excellent

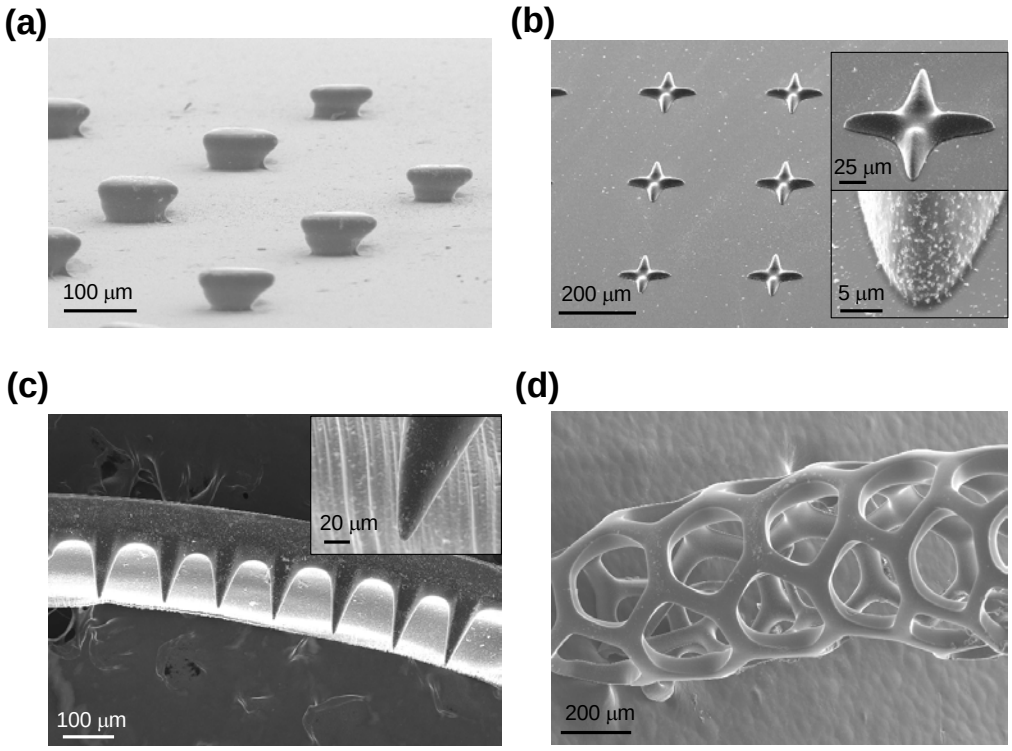

Figure 14. Various 3D structures fabricated by DOPsL including (a) a mushroom-like array, (b) a cross array, and (c) a tapered cantilever array (dark region – cantilever; light region - support). (d) A microtubule structure formed by releasing a honeycomb array from the substrate. The film rolls up after release due to slight stress gradients in the film.

transfer efficiencies of the digital mask to the solid polymer structures while still offering strong piezoelectric outputs and similar mechanical properties to the pure PEGDA materials. As the loading goes above 10 % the transparency of the polymer goes below 5 % at 365 nm which washes out the projected mask and causes shape distortions similar to what is observed in overexposed photoresists. Extinction spectra of the BTO nanoparticles clearly show the direct relationship between light-matter interactions and the BTO concentration (Figure 15). Higher loading fractions and better printing resolution should be attainable if tighter-focused light sources are used, the photopolymerization wavelength is tuned so that it falls in the higher transmission

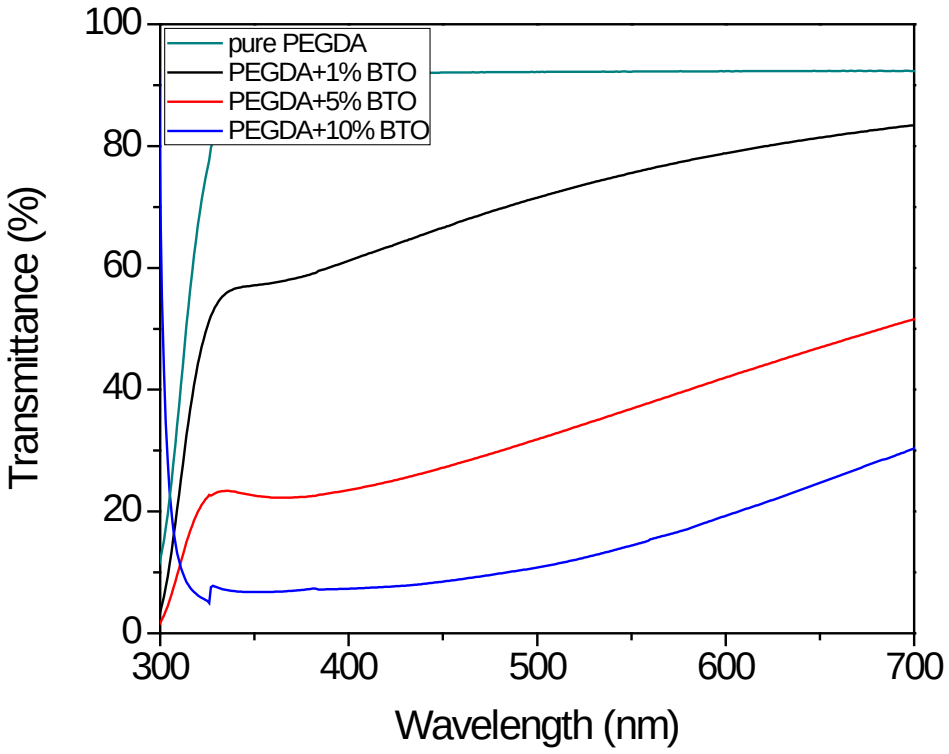

Figure 15. UV-Vis spectra of pure PEDGA (green) and PEGDA/BTO composite solutions; 1 % (black), 5 % (red), and 10% (blue). The transmittance is directly related to the BTO loading fraction and shows higher transmission at longer wavelength. The spectra were recorded using a Lambda 35 UV-Vis system (Perkin Elmer).

(longer wavelengths) region of the colloidal polymer solution, or the nanoparticle size is reduced; all of which will be topics of future research. In addition, smaller photopolymerization spots can be created using nonlinear optical processes such as two-photon absorption (TPA); however, high laser powers are required for multi-photon processes and the fabrication occurs via a much slower point-by-point scanning process.

2.3.3 Electrical Response

After photo-fabricating the composite materials, the printing cell can be used to activate the polymer. This requires that the dipoles in the perovskite crystallites be

aligned using a poling field that is larger than the coercive field (~ 10 V/μm) of the BTO nanoparticles. This was achieved using indium tin oxide (ITO) coated glass slides as the top and bottom electrodes, which also served as the top and bottom surface of the photofabrication cell. By placing an elastomeric spacer (e.g., PDMS or Kapton film) between the conductive glass substrates, the maximum height of the photofabricated structures is defined and precise electric fields could be applied to polarize the BTO nanoparticles. After activating the piezoelectric composite the fabricated films can either be left on the glass slides for testing and characterization, removed to create free-standing structures, or transferred to other substrates for further integration. If the photo-printing is carried out on a substrate that has weak interactions with the PEGDA composite (e.g., hydrophobic surface), the structured films can roll up to make higher order structures. The microtube shown in Figure 14d is one example where a honeycomb pattern is projected onto the nanoparticle composite solution and after polymerization the film is removed from the substrate which rolls up into a well-defined tubule. This process can be controlled by depositing bilayers with different thermal different thermal expansion coefficients, densities, or lattice parameters which would govern the diameter of the tube and extent of the rolling.[28]

The piezoelectric properties of the photofabricated materials were investigated by applying specific loads to neat (i.e., unstructured) photopolymerized films and measuring the electrical outputs with a home-built piezoelectric instrument (Chapter 1, Figure 6**)**. Neat films were investigated to ensure robust polymer-electrode interfaces, but the patterned microstructures (e.g., honeycomb array) also showed strong similar strong piezoelectric outputs after poling (Figure 17). Loads were applied orthogonal to the

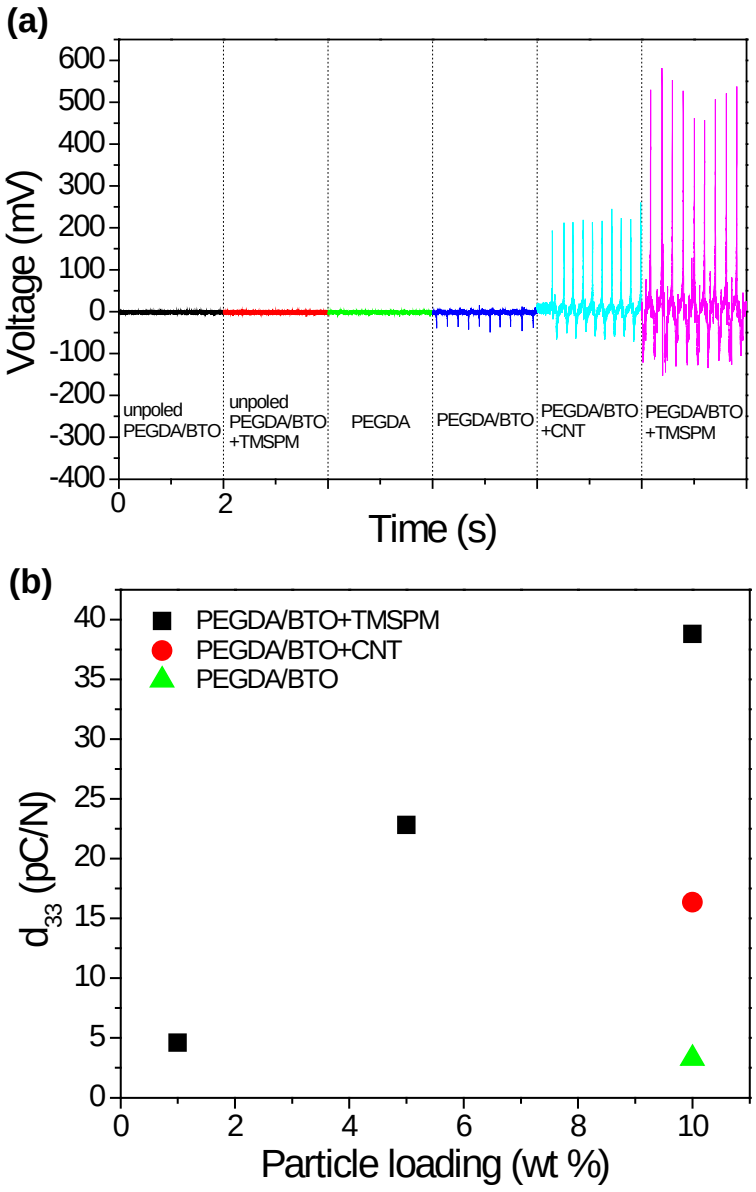

Figure 16. (a) Voltage response of various unpoled and poled composite materials (neat films) cycled with a 1.44 N load applied perpendicular to the surface of the film. Cycling data was collected for a total of 2 seconds for each film. (b) Plot showing the effective piezoelectric modulus (d_{33}) of a grafted PEGDA/BTO composite material as a function of BTO mass loading. The piezoelectric moduli for the 10% loaded PEGDA/BTO with CNTs and PEGDA/BTO (no CNTs or TMSPM) composites are also included for comparison.

substrate and the ITO-coated glass slides were used as top and bottom electrodes.

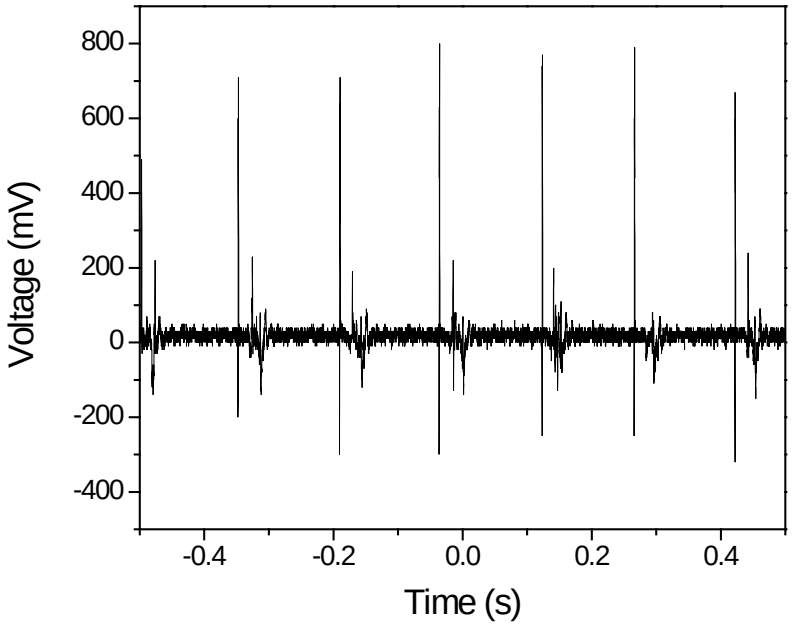

Figure 17. Voltage response of a 5% BTO loaded PEGDA honeycomb array (similar structure to Figure 2d) fabricated by DPP.

As expected, there is a significant enhancement in the cross-linked films that contain the TMSPM linker (no CNTs) compared to (1) the composite materials without the linker but with CNTs (1 % by mass) or (2) the composite with BTO nanoparticles only (no CNTs or TMSPM). In fact under similar loads (1.44 N) the composite films with the grafted nanoparticles displayed a > 2x boost in the piezoelectric output (Figure 16a) over the CNT composites and > 10x boost over composites without CNTs or TMSPM. There was no response from films fabricated with pure PEGDA, unpolarized composite materials containing TMSPM, or unpolarized composite materials without TMSPM. Quantifying the piezoelectric response of the 10 % BTO loaded CNT composites and TMSPM-grafted

composites gave effective piezoelectric coefficient (d_{33}) values of 13 ± 2 pC/N and 39 ± 3 pC/N, respectively. These values for the composites with grafted nanoparticles are already exceeding that of pure polymers such as PVDF which warrants further investigation into the upper limit of the photoliable composites and systematically studying the dependence of the piezoelectric properties on nanoparticle composition, polymer matrix, nanoparticle size, and linker chemistry.

The large increase in the piezoelectric coefficient is directly related to the mechanical interface between the BTO surface and PEGDA matrix which aids in the mechanical-to-electrical energy conversion process by efficiently funneling the stress in the polymer chains to the piezoelectric crystals. When no covalent linkages are formed between the nanoparticles and the polymer chains, the nanoparticles are just fillers and only weakly react to polymer deformations. The addition of CNTs helps stiffen the polymer matrix which increases the mechanical response of the piezoelectric nanoparticles when the polymer chains are strained. Future studies of this BTO-polymer chemical interface will be focused on how parameters such as grafting density, linker length, and polymer type affect the piezoelectric output of the composite materials. Although the piezoelectric properties of the polymer composites are lower than BTO monolithic ceramics (~ 200 pC/N), the composites are performing with a much lower density of active material while maintaining their mechanical flexibility. Analyzing the piezoelectric coefficient as a function of BTO mass loading (Figure 16b) shows a clear trend towards higher d_{33} values as the nanoparticle density increases. This upward trend should continue to increase and likely peak at a higher mass loading, but to reach the higher mass loading (> 10 %) the optical transparency of the colloidal solutions will have

to be improved. There are various ways to achieve this including reducing the size of the piezoelectric nanoparticles and/or photopolymerizing with longer wavelengths. The latter can be realized using TPA techniques or photoinitiators that absorbs deeper into the red/infrared regions.

2.4 Conclusions

Piezoelectric materials are key components in a range of devices including acoustic imaging, energy harvesting, and actuators, and typically rely on brittle ceramic monoliths to perform their functions. To control the size and or shape of the piezoelectrics it is common to use mechanical dicing or saws. However, this limits not only the size of the piezoelectric element but also the dimensionality. It is nearly impossible with current cutting techniques to shape brittle ceramics into higher order 3D structures which could have a huge impact on compact sensor designs, tunable acoustic arrays, efficient energy scavengers, and diagnostic devices. To address this issue we have demonstrated a novel tool for fabricating 3D piezoelectric materials that relies on piezoelectric nanoparticles embedded in a photoliable polymer solution. Digital optical masks generated by a programmable digital mirror device can project any user-defined pattern on the solution and in mere seconds the areas exposed to light photopolymerize leaving a solid structure after washing away the unexposed polymer. The proof-of-concept experiments were performed with BTO colloids mixed with PEGDA solutions, but the technology can easily be translated to other piezoelectric materials and polymers.

In addition to the DPP technology for printing 3D piezoelectric polymers, we introduced a novel means of enhancing the mechanical-to-electrical conversion process of nanocomposites. By chemically modifying the surface of the piezoelectric

nanoparticles with linker molecules that cross-link with the polymer matrix under light exposure, we formed direct covalent bonds with the polymer chains which helped channel the mechanical stresses from the deformed matrix through the piezoelectric nanoparticles. This boosted piezoelectric performance by over 10x and 2x compared to the composited fabricated without the linker molecules and those loaded with CNTs, respectively. The 3D printable resolution for the composite materials approached the ~ 1 μm limit using DPP, but this is solely governed by the light-matter interactions of the polymer solution and the spot size of the light source. Although not a focus of this work, there are various means of pushing the resolution down to diffraction-limited sizes which include the use of non-linear effects such as TPA and higher focusing components. Overall, these results are far reaching and should have immediate impact on a multitude of research fields including bioengineering, materials science, physics, and chemistry.

Chapter 2, in full, is a reprint of the material as it appears in ACS Nano 2014. Kim, K., Zhu, W., Qu, X., Aaronson, C., Chen, S., Sirbuly, D. J. are the co-authors of this material.

2.5 References

1 Jaffe, B.; Cook, W. R.; Jaffe, H., *Piezoelectric Ceramics*. Academic Press: London, 1971.

2 Fu, H. X.; Cohen, R. E., Polarization rotation mechanism for ultrahigh electromechanical response in single-crystal piezoelectrics. *Nature* **2000,** *403*, 281-283.

3 Karaki, T.; Yan, K.; Miyamoto, T.; Adachi, M., Lead-free piezoelectric ceramics with large dielectric and piezoelectric constants manufactured from BaTiO3 nano-powder. *Jpn. J. Appl. Phys., Part 2* **2007,** *46*, L97-L98.

4 Takahashi, H.; Numamoto, Y.; Tani, J.; Matsuta, K.; Qiu, J. H.; Tsurekawa, S., Lead-free barium titanate ceramics with large piezoelectric constant fabricated by microwave sintering. *Jpn. J. Appl. Phys., Part 2* **2006,** *45*, L30-L32.

5 Wada, S.; Yako, K.; Kakemoto, H.; Tsurumi, T.; Kiguchi, T., Enhanced piezoelectric properties of barium titanate single crystals with different engineered-domain sizes. *J. Appl. Phys.* **2005,** *98*.

6 Kawai, H., Piezoelectricity of poly (vinylidene fluoride). *Jpn. J. Appl. Phys.* **1969,** *8*, 975-976.

7 Hu, Z.; Tian, M.; Nysten, B.; Jonas, A. M., Regular arrays of highly ordered ferroelectric polymer nanostructures for non-volatile low-voltage memories. *Nature Mater.* **2009,** *8*, 62-67.

8 Foster, F. S.; Harasiewicz, E. A.; Sherar, M. D., A history of medical and biological imaging with polyvinylidene fluoride (PVDF) transducers. *IEEE Trans. Ultrason., Ferroelect., Freq. Contr.* **2000,** *47*, 1363-1371.

9 Harris, G. R.; Preston, R. C.; DeReggi, A. S., The impact of piezoelectric PVDF on medical ultrasound exposure measurements, standards, and regulations. *IEEE Trans. Ultrason., Ferroelect., Freq. Contr.* **2000,** *47*, 1321-1335.

10 Wang, F.; Tanaka, M.; Chonan, S., Development of a PVDF piezopolymer sensor for unconstrained in-sleep cardiorespiratory monitoring. *J. Intell. Mater. Syst. Struct.* **2003,** *14*, 185-190.

11 Lee, S.; Bordatchev, E. V.; Zeman, M. J. F., Femtosecond laser micromachining of polyvinylidene fluoride (PVDF) based piezo films. *J. Micromech. Microeng.* **2008,** *18*.

12 Alexe, M.; Harnagea, C.; Hesse, D.; Gosele, U., Patterning and switching of nanosize ferroelectric memory cells. *Appl. Phys. Lett.* **1999,** *75*, 1793-1795.

13 Ganpule, C. S.; Stanishevsky, A.; Aggarwal, S.; Melngailis, J.; Williams, E.; Ramesh, R.; Joshi, V.; de Araujo, C. P., Scaling of ferroelectric and piezoelectric properties in $Pt/SrBi_2Ta_2O_9/Pt$ thin films. *Appl. Phys. Lett.* **1999,** *75*, 3874-3876.

14 Chang, L. W.; McMillen, M.; Morrison, F. D.; Scott, J. F.; Gregg, J. M., Size effects on thin film ferroelectrics: Experiments on isolated single crystal sheets. *Appl. Phys. Lett.* **2008,** *93*, 132904.

15 Nagarajan, V.; Stanishevsky, A.; Ramesh, R., Ferroelectric nanostructures via a modified focused ion beam technique. *Nanotechnology* **2006,** *17*, 338-343.

16 Xia, Y. N.; Whitesides, G. M., Soft lithography. *Annu. Rev. Mater. Sci.* **1998,** *28*, 153-184.

17 Alexe, M.; Gruverman, A.; Harnagea, C.; Zakharov, N. D.; Pignolet, A.; Hesse, D.; Scott, J. F., Switching properties of self-assembled ferroelectric memory cells. *Appl. Phys. Lett.* **1999,** *75*, 1158-1160.

18 Chang, C. E.; Tran, V. H.; Wang, J. B.; Fuh, Y. K.; Lin, L. W., Direct-Write Piezoelectric Polymeric Nanogenerator with High Energy Conversion Efficiency. *Nano Lett.* **2010,** *10*, 726-731.

19 Gallego-Perez, D.; Ferrell, N. J.; Higuita-Castro, N.; Hansford, D. J., Versatile methods for the fabrication of polyvinylidene fluoride microstructures. *Biomed. Microdevices* **2010,** *12*, 1009-1017.

20 Arcaute, K.; Mann, B. K.; Wicker, R. B., Stereolithography of three-dimensional bioactive poly(ethylene glycol) constructs with encapsulated cells. *Ann. Biomed. Eng.* **2006,** *34*, 1429-1441.

21 Han, L.-H.; Suri, S.; Schmidt, C. E.; Chen, S., Fabrication of three-dimensional scaffolds for heterogeneous tissue engineering. *Biomed. Microdevices* **2010,** *12*, 721-725.

22 Mapili, G.; Lu, Y.; Chen, S. C.; Roy, K., Laser-layered microfabrication of spatially patterned functionalized tissue-engineering scaffolds. *J. Biomed. Mater. Res. Part B Appl. Biomater.* **2005,** *75B*, 414-424.

23 Zorlutuna, P.; Annabi, N.; Camci-Unal, G.; Nikkhah, M.; Cha, J. M.; Nichol, J. W.; Manbachi, A.; Bae, H.; Chen, S.; Khademhosseini, A., Microfabricated Biomaterials for Engineering 3D Tissues. *Adv. Mater.* **2012,** *24*, 1782-1804.

24 Chen, D. R.; Jiao, X. L., Solvothermal synthesis and characterization of barium titanate powders. *J. Am. Ceram. Soc.* **2000,** *83*, 2637-2639.

25 Park, K.-I.; Lee, M.; Liu, Y.; Moon, S.; Hwang, G.-T.; Zhu, G.; Kim, J. E.; Kim, S. O.; Kim, D. K.; Wang, Z. L.; Lee, K. J., Flexible Nanocomposite Generator Made of BaTiO3 Nanoparticles and Graphitic Carbons. *Adv. Mater.* **2012,** *24*, 2999-3004.

26 Xu, S.; Yeh, Y.-w.; Poirier, G.; McAlpine, M. C.; Register, R. A.; Yao, N., Flexible Piezoelectric PMN-PT Nanowire-Based Nanocomposite and Device. *Nano Lett.* **2013,** *13*, 2393-2398.

27 Zhang, A. P.; Qu, X.; Soman, P.; Hribar, K. C.; Lee, J. W.; Chen, S.; He, S., Rapid Fabrication of Complex 3D Extracellular Microenvironments by Dynamic Optical Projection Stereolithography. *Adv. Mater.* **2012,** *24*, 4266-4270.

28 Schmidt, O. G.; Eberl, K., Nanotechnology - Thin solid films roll up into nanotubes. *Nature* **2001,** *410*, 168-168.

29 Lee, H.-W.; Moon, S.; Choi, C.-H.; Kim, D. K., Synthesis and Size Control of Tetragonal Barium Titanate Nanopowders by Facile Solvothermal Method. *J. Am. Ceram. Soc.* **2012,** *95*, 2429-2434.

30 Du, M.; Zheng, Y., Modification of silica nanoparticles and their application in UDMA dental polymeric composites. *Polym. Compos.* **2007,** *28*, 198-207.